NACA RM L55F23

NACA

RESEARCH MEMORANDUM

AERODYNAMIC CHARACTERISTICS AT MACH NUMBERS FROM 0.7 TO 1.75 OF A FOUR-ENGINE SWEPT-WING AIRPLANE CONFIGURATION AS OBTAINED FROM A ROCKET-PROPELLED MODEL TEST

By Rowe Chapman, Jr.

Langley Aeronautical Laboratory
Langley Field, Va.

CLASSIFIED DOCUMENT

This material contains information affecting the National Defense of the United States within the meaning of the espionage laws, Title 18, U.S.C., Secs. 793 and 794, the transmission or revelation of which in any manner to an unauthorized person is prohibited by law.

NATIONAL ADVISORY COMMITTEE
FOR AERONAUTICS

WASHINGTON

September 2, 1955

NATIONAL ADVISORY COMMITTEE FOR AERONAUTICS

RESEARCH MEMORANDUM

AERODYNAMIC CHARACTERISTICS AT MACH NUMBERS FROM 0.7 TO 1.75 OF A FOUR-ENGINE SWEPT-WING AIRPLANE CONFIGURATION AS OBTAINED FROM A ROCKET-PROPELLED MODEL TEST

By Rowe Chapman, Jr.

SUMMARY

A rocket-propelled model typical of multiengine airplane configurations has been flight tested to obtain data on drag, stability, and nacelle performance. The model wing had an aspect ratio of 3.5, a sweepback of 47° at the quarter chord line, and a taper ratio of 0.2. Four nacelles were closely coupled underneath the wing at the 40- and 70-percent semispan positions. Data were obtained for Mach numbers from 0.70 to 1.8 and lift coefficients from 0 to 0.4 at subsonic speeds and from -0.05 to 0.12 at supersonic speeds. These data are compared with previously unpublished wind-tunnel data from similar configurations.

The model experienced a nose-down trim change in angle of attack of the order of $1\frac{1}{2}^\circ$ in going from subsonic to supersonic speeds at low lift conditions with the magnitude of the change increasing to 4° for the higher lift condition. The configuration had a minimum drag coefficient of 0.035 at supersonic speeds with maximum lift-drag ratios of 13.2 and 4 at subsonic and supersonic speeds. Nacelles had mass-flow ratios and pressure recoveries that deteriorated from near 1.0 at $M = 0.75$ to respective minimums of 0.64 and 0.63 near a Mach number of 1.35 and then increased consistently with increasing Mach numbers.

The longitudinal static stability derivative was essentially invariant with lift coefficient except in the Mach number range from 0.92 to 1.08; however no pitch-up was encountered in this region.

INTRODUCTION

A rocket-propelled model has been flight tested in a continued program to determine the drag, stability, and nacelle performance characteristics of airplane configurations. The model of the present test had a

47° swept wing at an incidence of 4° and a conventional empennage group that also had swept surfaces. Four nacelles were closely coupled beneath the wing at the 40 and 70 percent semispan positions. The high-fineness-ratio fuselage incorporated a canopy and an upswept rear portion.

The flight test was conducted at the Pilotless Aircraft Research Station, Wallops Island, Va. Results from the flight test are compared with unpublished data from tunnel tests of similar configurations.

SYMBOLS

C_N	normal-force coefficient, $\left(\frac{A_n}{g}\right)\left(\frac{W}{qS}\right)$
C_C	chord-force coefficient, $\left(\frac{A_l}{g}\right)\left(\frac{W}{qS}\right)$
C_L	lift coefficient, $C_N \cos \alpha - C_C \sin \alpha$
C_D	drag coefficient, $C_C \cos \alpha + C_N \sin \alpha$
C_m	pitching-moment coefficient
A_n/g	normal acceleration as obtained from accelerometer, g units
A_l/g	longitudinal acceleration as obtained from accelerometer, g units
W	model weight
g	acceleration of gravity, ft/sec^2
V	velocity, ft/sec
q	dynamic pressure, $\frac{\gamma}{2} pM^2$, lb/sq ft
M	Mach number
γ	specific heat ratio for air (1.40)
S	basic wing area (including area within the fuselage), 5.47 sq ft

R	Reynolds number, based on wing mean aerodynamic chord
b	wing span
$\bar{c}$	wing mean aerodynamic chord, ft
x	longitudinal distance along body axis from nose, in.
r_e	radius of equivalent body of revolution, in.
A	cross-sectional area in plane normal to body axis, $in.^2$
l	body length, in.
I_Y	moment of inertia about Y-axis, $slug\text{-}ft^2$
I_X	moment of inertia about X-axis, $slug\text{-}ft^2$
I_Z	moment of inertia about Z-axis, $slug\text{-}ft^2$ (assumed equal to I_Y)
α	angle of attack, deg
θ	angle of pitch, radians
δ	incidence of horizontal tail, deg
P	period of oscillation, sec
t	time, sec
$\dot{\alpha}$	rate of change of angle of attack, $\frac{1}{57.3}\frac{d\alpha}{dt}$, radians/sec
q	rate of change of angle of pitch, $\frac{d\theta}{dt}$, radians/sec

$$C_{m_q} = \frac{dC_m}{d\left(\frac{q\bar{c}}{2V}\right)} \text{ per radian}$$

$$C_{m_{\dot{\alpha}}} = \frac{dC_m}{d\left(\frac{\dot{\alpha}\bar{c}}{2V}\right)} \text{ per radian}$$

$C_{n_\beta}{}^*$	static directional stability derivative obtained from $C_{n_\beta} = 4\pi I_Z / qSbP^2$
p	static pressure of undisturbed free stream, lb/sq in.
p_o	standard sea-level static pressure, lb/sq in.
$T_{1/2}$	time to damp to one-half amplitude, sec
H	total pressure of undisturbed free stream, lb/sq in. abs
m	mass flow through stream tube
X_n	distance along nacelle measured from nose, in.
L_n	length of nacelle, in.

Subscripts:

T	trimmed or mean value
d	duct
e	exit
i	internal

The symbols α and δ used as a subscript indicate the derivatives of the quantity with respect to the subscript.

MODEL AND INSTRUMENTATION

Model Description

The general arrangement of the model is shown in the drawing of figure 1(a). Table I gives the characteristics of the surfaces as well as the mass and inertia characteristics of the model. Airfoil ordinates are given in table II and the tail contour ordinates are given in table III. A detailed drawing of the close-coupled underslung nacelles is shown in figure 1(b) with the location of the static-pressure orifices noted on the figure as p_d (duct pressure) and p_e (pressure at the exit). The static pressures were taken at only one annular position in the left inboard nacelle of the model.

The geometric relationships between the model and its equivalent body of revolution at $M = 1.0$ are shown in the area distribution plot of figure 1(c). Photographs of the model alone are shown in figures 2(a) and 2(b).

All metal construction was utilized for the model with aerodynamic surfaces made of aluminum alloy. The all-movable horizontal tail was pulsed in a programmed square wave motion between incidences of -3.47° and 0.13°. All angles of attack and angles of incidence are given with reference to the center line of the cylindrical portion of the fuselage.

Instrumentation

The model contained an eleven-channel, shock-mounted, tray-type NACA telemeter. Continuous measurements of normal acceleration at the nose of the model, normal acceleration at the center of gravity of the model, transverse acceleration at the center of gravity, longitudinal acceleration (high range), longitudinal acceleration (low range), angle of attack, horizontal-tail incidence, total pressure, base pressure behind angle-of-attack indicator, static pressure in nacelle duct, and static pressure at nacelle exit were made.

Model position in space was determined by NACA modified SCR 584 tracking radar and model velocity was obtained by use of the CW Doppler velocimeter. Atmospheric data were obtained from rawinsonde measurements.

TEST AND ANALYSIS

Test

The model was launched at an elevation of approximately 60° from a mobile launcher. Figure 2(c) is a photograph of the model on the launcher and shows the model in relation to its underslung booster.

The underslung booster utilized two 6-inch-diameter ABL rocket motors for propelling the combination to a maximum Mach number of 1.8. Canted nozzles were used on the booster to aline the thrust axis through the vertically displaced center of gravity of the combination at take-off. The model was positioned so that the wing had an incidence of 2° with respect to the center line of the rocket motors (booster fins had zero incidence) with the horizontal tail of the model positioned so that the model would be released in the trimmed (high lift) attitude if the combination was at zero angle of attack at separation. In order to insure a favorable drag-weight ratio of model relative to the booster, a deceleration actuated drag flap located underneath the rear box of the booster was used.

Velocity data were obtained from the CW Doppler radar for 12 seconds of the flight, corresponding to the supersonic portion of the data. For the remaining portion of the flight, Mach number and dynamic pressure were computed utilizing the total-pressure measurement and checked by use of velocity obtained from integration of the acceleration tangent to the flight path. Velocity data from the radar were corrected for the curved flight path and other data corrections were applied in accordance with the procedures discussed in references 1 and 2. Static pressure of the free stream was obtained by use of the radar position data with the rawinsonde data.

Test conditions are shown by the plots of figure 3, where the Reynolds number is based on the wing mean aerodynamic chord.

Analysis

The analyses made were based on the methods presented in reference 1. There were no indications in the data that the conditions of the two-degree-of-freedom assumption in the analysis procedure were violated.

ACCURACY

These telemetered data are believed to be accurate within ±1 percent of the full-scale range of the respective instruments. Errors of these magnitudes when converted to probable errors in the final coefficients and quantities are given for the respective Mach numbers in the following table:

M	Percent C_L	Percent C_D	Nacelle Δp	Absolute $\Delta\alpha$	Incremental $\Delta\alpha$
0.8	5.2	5.2	±0.29	1/2°	±0.18°
1.7	2.45	2.45	±0.29	1/2°	±0.18°

A portion of the errors in the aforementioned table is introduced by possible errors in dynamic pressure. This type of error was accentuated by the failure to obtain velocimeter data for the lower Mach number regions of the flight. The probable error in dynamic pressure is estimated to vary from 1.75 percent at maximum supersonic speeds to 4.8 percent at $M = 0.80$. The possible error in Mach number for this model is of the order of ±0.02 in the regions below Mach number 1.2 and less at higher Mach numbers.

RESULTS AND DISCUSSION

The data presented in figures 4 to 21 obtained in the present test of a rocket-propelled model are compared with unpublished data from wind-tunnel test of a similar configuration. The data from the rocket-model test cover lift-coefficient ranges from 0 to 0.40 in the subsonic region. In the supersonic region, lift coefficients covered in the test ranged from -0.05 to 0.12.

Airplane Performance

Trim.- The deflection of the tail in an approximate square-wave produced regions of data for alternate tail incidences of -3.47° and 0.13°. Trim angle of attack and trim lift coefficient are plotted in figure 4 for the center-of-gravity location of 27.4 percent mean aerodynamic chord. The trim C_L required for level flight at sea level and wing loading of 100 pounds per square foot (typical for full-scale configurations) follows closely the model trim C_L for $\delta = 0.13^\circ$ as shown in the figure. The correspondence of the required C_L for level flight at 35,000 feet altitude to the model trim for $\delta = 3.47^\circ$ is also shown in the figure.

The model had a nose-down trim change of $1\frac{1}{2}^\circ$ in going from subsonic to supersonic speeds for the tail setting of $\delta = 0.13^\circ$. At the tail setting of -3.47° the model experienced nose-down trim changes of the order of 4° in going from subsonic to supersonic speeds.

Lift.- The basic data plots of lift as a function of the angle of attack are presented in figure 5. In figure 6 the lift-curve slopes are shown as a function of Mach number with curves from the tunnel test for a comparable model also presented.

In the transonic ranges, the lift-curve slope is essentially invariant with angle of attack below $M = 0.95$, but the level obtained from the present test is lower than that obtained in the tunnel test. These lower lift-curve slopes obtained in the present test are comparable to a certain extent to the results of reference 3 wherein large decreases in lift-curve slope are shown to occur for low positive angles of attack when afterbody upsweep is used. The tunnel model tested had no upswept fuselage because of the sting mount requirements.

At the supersonic Mach numbers the C_{L_α} values obtained are comparable with those obtained from the tunnel test with the lift-curve

slopes from the present test being slightly lower at the higher lift coefficients for Mach numbers above 1.25.

Drag.- Plots of basic drag data are presented in figure 7. The drag polars were obtained when the incidence of the horizontal tail was held constant at one of the two positions while the lift coefficient was varied. The true drag coefficient at trimmed lift can be obtained by cross reference of figure 4 and figure 7.

The variation of minimum drag with Mach number is shown in figure 8. During the drag rise, beginning at $M = 0.95$, data points were plotted directly from the time history for the low lift condition (this gives an incremental C_D due to a small value of lift, but removes the greater effect of the varying Mach number). The supersonic level of $C_{D_{min}}$ (0.035) of the configuration having close-coupled underslung nacelles is midway between that of 0.03 for the buried-nacelle configuration and 0.04 for the cone-pod nacelle configuration obtained from the tunnel tests.

Plots of L/D as a function of lift coefficient are shown in figure 9. The maximum lifts attained by the model were higher than the C_L for maximum L/D at subsonic Mach numbers. At supersonic Mach numbers the C_L for maximum L/D was not reached and hence the maximums are extrapolated from a fitted parabola. The extrapolated $(L/D)_{max}$ points shown for the subsonic Mach numbers were calculated using the C_L for minimum C_D from the $\delta = +0.13^\circ$ tail setting and the variation of drag with lift for the higher lift regions.

Presented in figure 10(a) is the variation with Mach number of values obtained for $(L/D)_{max}$ utilizing data from the present test. The data from the unpublished tunnel tests presented in figure 10(a) compared with data in the present report indicate an untrimmed $(L/D)_{max}$ of about 4 at Mach numbers above 1.5 for configurations having exposed nacelles. Data from the present test show an untrimmed $(L/D)_{max}$ of 13.2 at $M = 0.90$ for the configuration having close-coupled underslung nacelles.

The C_L optimum, or C_L for maximum (L/D), are presented in figure 10(b). Data from all sources show essential agreement on a subsonic level of approximately 0.25 and a supersonic level of 0.26 above $M = 1.7$.

Nacelle Performance

Two static pressures were measured within the left inboard nacelle at the nacelle stations shown in figure 1(b). The basic data plot of static pressure at the exit and in the duct are presented in figure 11 as a function of time. For reference, free-stream total pressure, static pressure, and Mach number are also shown in figure 11.

The internal pressures are shown as point values to indicate the effects of the constantly changing angle of attack. Although some slight trends may be indicated at the low Mach numbers, where the trim angle of attack spread is greater (fig. 4), in general, the angle-of-attack effects are very small and not considered further herein.

The total-pressure recovery, mass-flow ratio, and internal-drag coefficient were determined using faired values of the internal pressures and are presented in figure 12 as functions of Mach number. Isentropic channel flow equations with the pressure and area ratios were used to calculate all data presented in figure 12.

These data indicate that the nacelles have pressure recovery factors and mass-flow ratios near 1.0 at $M = 0.75$ with a deterioration in efficiency at transonic Mach numbers followed by increased efficiency for $M > 1.35$. Extrapolation of the data indicates that these ratios would approach 1.0 again near $M = 2.3$. These values are compatible with the fact that the concial shock from the island should be detached at Mach numbers less than 1.35 and would intersect the cowl lip for a Mach number of slightly over 2.00. Magnitudes of the nacelle parameters of the present tests agree well with those in tunnel tests of a comparable nacelle. For example, at $M = 1.41$, the mass-flow ratio and C_{D_i} calculated from data of the present test were 0.65 and 0.00065, respectively. For the same Mach number, tunnel data gave values of 0.68 and 0.0006, respectively, for the similar nacelle.

Figure 13 is a reproduction of a portion of the telemeter record and shows the buzzing of the duct static pressure that occurred only during the higher lift oscillations. The buzz is first detectable near $M = 1.18$. The following chart indicates the frequency Mach number relationship of the buzzing:

M	Frequency, cps	M	Frequency, cps
1.18	180	0.97	140
1.12	115	0.92	205
1.05	None	0.88	250
0.99	115		

As the Mach number further decreases, the frequency apparently increases but becomes difficult to discern.

Longitudinal Characteristics

Static stability.- The measured period of the short-period longitudinal oscillation is presented in figure 14. There appears to be no difference in period between the low lift and the higher lift conditions for $M > 1.1$. Below $M = 1.1$ separate lines are faired for the period at the different tail settings.

Presented in figure 15 are the C_{m_α} values computed from the faired period curves of figure 14 utilizing the usual two-degree-of-freedom relations. There is very little stability change in going from the low lift to the higher lift below Mach number of 0.92 and above Mach numbers of 1.08. For the Mach number range of 0.92 to 1.08 a distinct stability change is noted with the configuration being more stable at the higher lifts. No regions of pitch-up were encountered in this test.

A plot of aerodynamic center is shown in figure 16 as obtained from plots of $A_{n_{nose}}$ against $A_{n_{cg}}$. Also shown in figure 16 are plots of aerodynamic center as obtained using the C_{m_α} from the period with the lift-curve slopes presented in figure 6. This agreement between the two methods is good.

Horizontal-tail effectiveness.- The effectiveness of the horizontal tail for producing pitching moments is shown as a function of Mach number in figure 17. The data points were obtained by using the pitching moments from the two normal accelerations in the regions where the rapid change of the longitudinal tail incidence took place. The lag in model response allowed the introduction of only small errors due to nonlinear C_{m_α} values since the $\Delta\alpha$ for all computations was less than 0.4° for a full range change of tail incidence (3.60°). The solid line presented in figure 17 was obtained using the $(\alpha/\delta)_T$ values with the corresponding C_{m_α} value. This represents a definite averaging process if there are nonlinearities present.

The spread in trim curves shown in figure 4 shows the horizontal-tail effectiveness for producing changes in angle of attack. These data indicate that the horizontal tail is approximately one-third as effective at supersonic speeds as at subsonic speeds.

Dynamic stability.- The time required for the transient oscillation to damp to one-half amplitude is presented in figure 18. These damping

data have little scatter except at Mach numbers of 0.78, 0.97, and 1.23 where there is evidence of irregularities. The reduction of this type of data and possible irregularities are discussed in reference 4.

The sum of the longitudinal damping derivatives $(C_{m_q} + C_{m_{\dot{\alpha}}})$ is presented in figure 19. These data were obtained from the faired curves of figure 18. At the low lift condition near $M = 1.0$ the sum of the damping derivatives is slightly on the unstable side; however, there was still damping of the oscillation due to the damping contribution of C_{L_α}. Variation of the damping-moment derivatives with Mach number is highly irregular below $M = 1.1$ as is the case for a number of swept-wing configurations (ref. 4). Above $M = 1.1$ the value of $(C_{m_q} + C_{m_{\dot{\alpha}}})$ tends to show a smooth variation between the values of -5 and -7.5.

Lateral Characteristics

Static stability.- The variation of the period of the side-force oscillation with time is shown in figure 20. These oscillations were very low amplitude disturbances in the lateral plane. Since the model was primarily a longitudinal model the moment of inertia in yaw was not measured. In order to reduce the lateral period data it was assumed that the moment of inertia in yaw was equal to the measured moment of inertia in pitch. The static stability derivative $C_{n_\beta}{}^*$ obtained from a single-degree-of-freedom analysis of the faired period curve of figure 20 are presented in figure 21 as a function of Mach number. The data from the tunnel test are also shown in the figure. Experience has shown that, for rocket models, I_Z is greater than I_Y by about 5 to 10 percent for models with no nacelles. With nacelles this difference should be even greater. Since the measurement of $C_{n_\beta}{}^*$ was a secondary quantity no detailed study was made to explain the differences; however, it appears that the increased I_Z, a more refined consideration of the data, and inclusion of the effect of the fuselage modification in the tunnel model could possibly explain the indicated differences in lateral stability.

CONCLUSIONS

A free-flight test of a rocket model representative of swept-wing multiengine configurations has been made for Mach numbers from 0.70 to 1.80. Lift coefficients for the test ranged from 0 to 0.40 at subsonic speeds and from -0.05 to 0.12 at supersonic speeds. From an analysis of the data the following conclusions are indicated:

1. Nose-down trim changes of the order of $1\frac{1}{2}^{\circ}$ were encountered in going from subsonic to supersonic Mach numbers at the lower lift conditions. The trim changed about 4°, nose down, at the higher lifts in going from subsonic to supersonic speeds.

2. Although lift-curve slopes compare favorably at supersonic speeds with previous results, the rocket model having an upswept fuselage showed markedly lower lift-curve slopes at a Mach number of 0.80 ($M = 0.80$) than did a comparable wind-tunnel model.

3. The configuration has a minimum drag coefficient of 0.035 at supersonic speeds and a drag rise beginning at a Mach number of 0.95. The maximum lift-drag ratio decreased from 13.2 at $M = 0.90$ to about 4 at supersonic speeds.

4. Nacelle pressure measurements indicated mass-flow ratios and pressure-recovery factors near 1.0 at $M = 0.75$ with a general deterioration in efficiency up to $M = 1.35$ where minimum values of 0.64 and 0.63 occur. Above $M = 1.35$ a consistent increase in efficiency occurs with an increase in speed.

5. The longitudinal static stability derivative is essentially invariant with lift coefficient except in the Mach number range from 0.92 to 1.08. In this region the stability increased slightly with lift coefficient. No pitch-up regions were encountered in the test.

6. The horizontal tail was approximately one-third as effective at supersonic speeds as at subsonic speeds for changing the trim angle of attack.

7. The sum of the longitudinal damping-moment derivatives shows irregular variations in the transonic regions with slightly unstable values near $M = 1.0$. At Mach numbers greater than 1.10 the damping-moment coefficient shows a smooth variation with Mach number between values of -5 and -7.5.

Langley Aeronautical Laboratory,
National Advisory Committee for Aeronautics,
Langley Field, Va., June 15, 1955.

REFERENCES

1. Gillis, Clarence L., Peck, Robert F., and Vitale, A. James: Preliminary Results From a Free-Flight Investigation at Transonic and Supersonic Speeds of the Longitudinal Stability and Control Characteristics of an Airplane Configuration With a Thin Straight Wing of Aspect Ratio 3. NACA RM L9K25a, 1950.

2. Ikard, Wallace L.: An Air-Flow-Direction Pickup Suitable for Telemetering Use on Pilotless Aircraft. NACA RM L53K16, 1954.

3. Parks, James H.: Transonic Longitudinal Aerodynamic Effects of Sweeping Up the Rear of the Fuselage of a Rocket-Propelled Airplane Model Having No Horizontal Tail. NACA RM L54K12, 1954.

4. Gillis, Clarence L., and Chapman, Rowe, Jr.: Summary of Pitch-Damping Derivatives of Complete Airplane and Missile Configurations as Measured in Flight at Transonic and Supersonic Speeds. NACA RM L52K20, 1953.

TABLE I

PHYSICAL CHARACTERISTICS OF THE MODEL

Wing:	
Area (included), sq ft	5.48
Span, ft	4.38
Aspect ratio	3.5
Mean aerodynamic chord, ft	1.433
Sweepback (1/4c), deg	47
Dihedral (relative to mean thickness line), deg	0
Taper ratio	0.20
Horizontal tail:	
Area (included), sq ft	0.667
Aspect ratio	3.52
Span	1.532
Mean aerodynamic chord, ft	0.50
Sweepback (leading edge, 1/4c), deg	47
Taper ratio	0.20
Vertical tail:	
Area (extended to model center line), sq ft	0.432
Aspect ratio	1.480
Height (above center line of model), ft	0.80
Sweepback (leading edge, 1/4c)	47
Taper ratio	0.20
Mass and inertia:	
Weight, lb	136.8
Center-of-gravity position, percent M.A.C.	27.5
Moment of inertia, pitch, slug-ft^2	8.72
Moment of inertia, roll, slug-ft^2	1.72

TABLE II

WING CONTOUR ORDINATES

[Measured above and below chord line]

Station, percent chord	Upper surface ordinate, percent chord	Lower surface ordinate, percent chord
0	0.05	0
.5	.53	.33
2.5	1.22	.54
5.0	1.76	.65
10.0	2.50	.86
20.0	3.26	1.28
30.0	3.62	1.61
40.0	3.73	1.76
50.0	3.58	1.74
60.0	3.14	1.47
70.0	2.47	1.14
80.0	1.69	.80
90.0	.91	.45
100.0	.12	.12

WING TWIST

[Trailing edge of airfoil is in wing root plane at all stations]

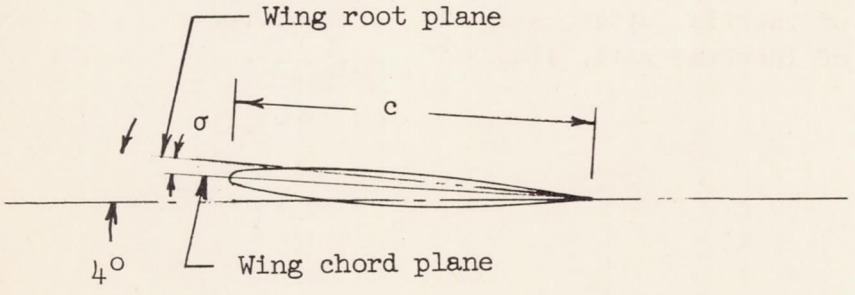

	40-percent-semispan station	Tip station
c	16.998 in.	5.107 in.
σ	0°14'29"	2°26'

TABLE III

HORIZONTAL AND VERTICAL TAIL CONTOUR ORDINATES

[Measured above and below chord line]

Station, percent chord	Upper and lower surface ordinates, percent chord
0	0
.5	.436
.75	.526
1.25	.657
2.5	.876
5.0	1.201
7.5	1.456
10.0	1.672
15.0	2.014
20.0	2.275
25.0	2.472
30.0	2.614
35.0	2.706
40.0	2.748
45.0	2.734
50.0	2.658
55.0	2.512
60.0	2.308
65.0	2.059
70.0	1.774
75.0	1.478
80.0	1.183
85.0	.887
90.0	.591
95.0	.296
100.0	0

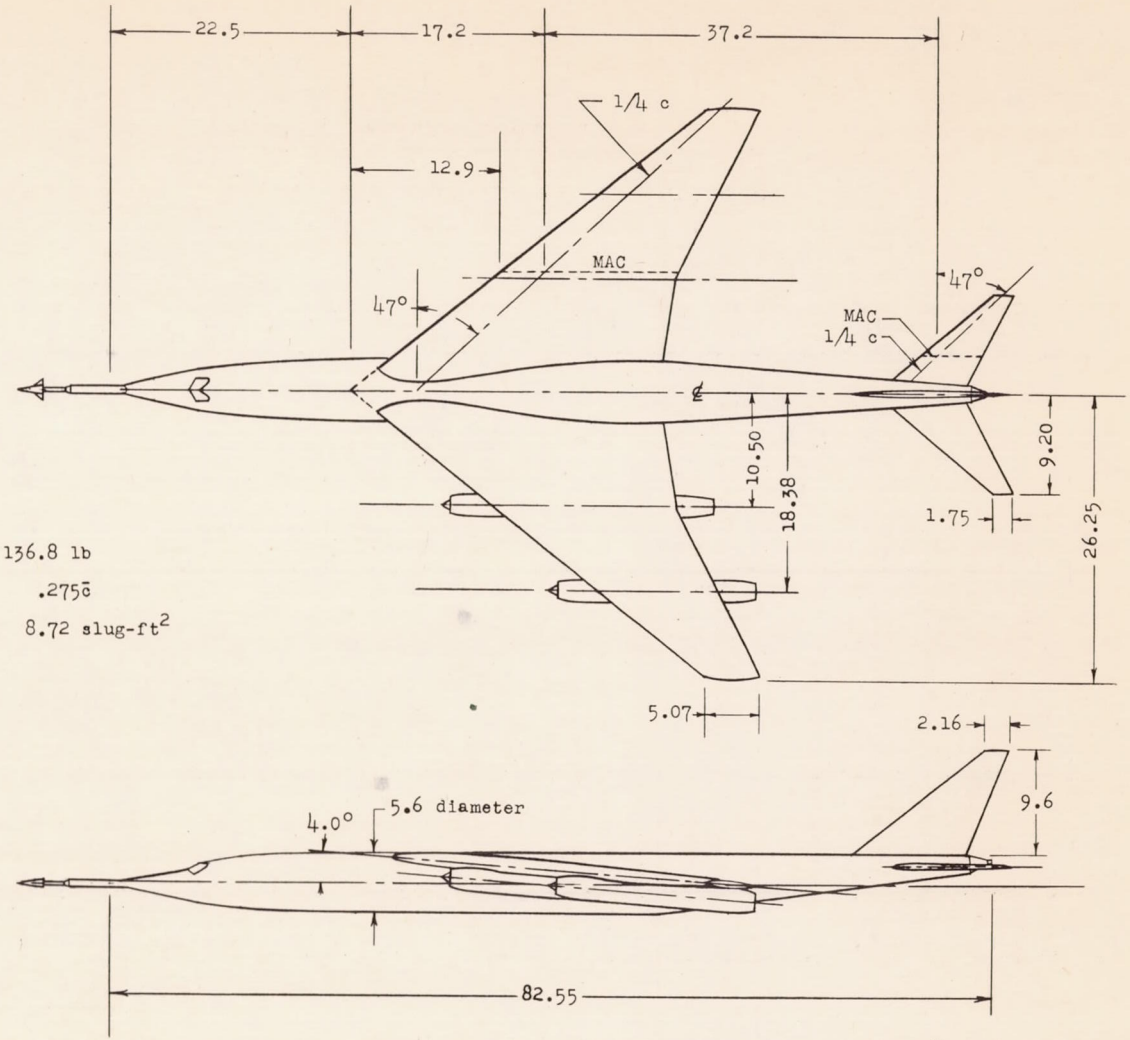

Weight	136.8 lb
Center of gravity location	.275$\bar{c}$
Moment of inertia in pitch	8.72 slug-ft^2

(a) Drawing of the model. All dimensions are in inches.

Figure 1.- Geometric and mass characteristics of the model.

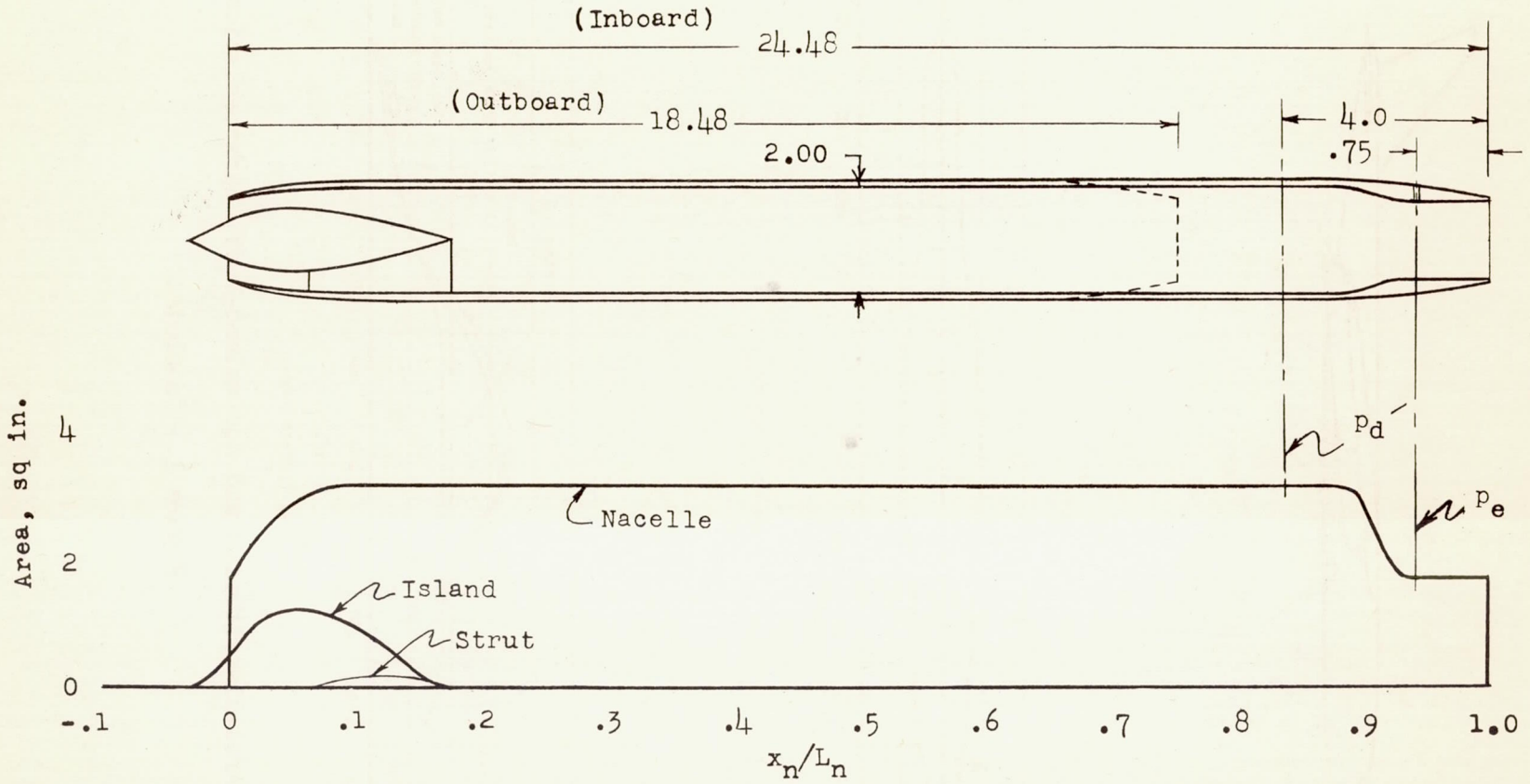

(b) Nacelle characteristics. Air-flow area included.

Figure 1.- Continued.

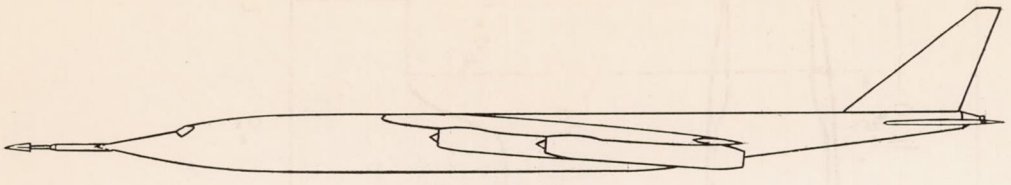

Model

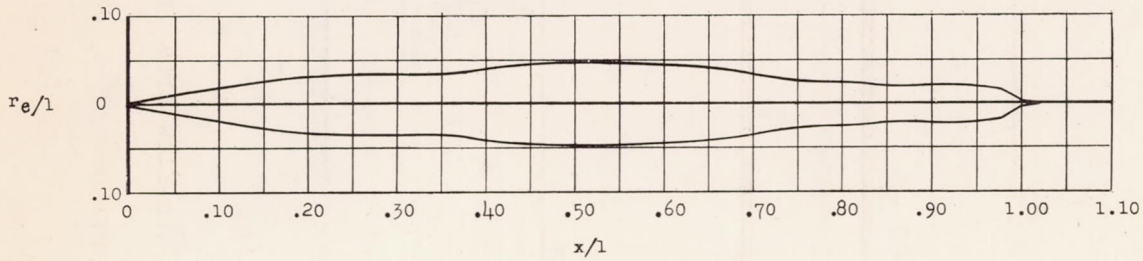

Equivalent body

l = 82.55 in.

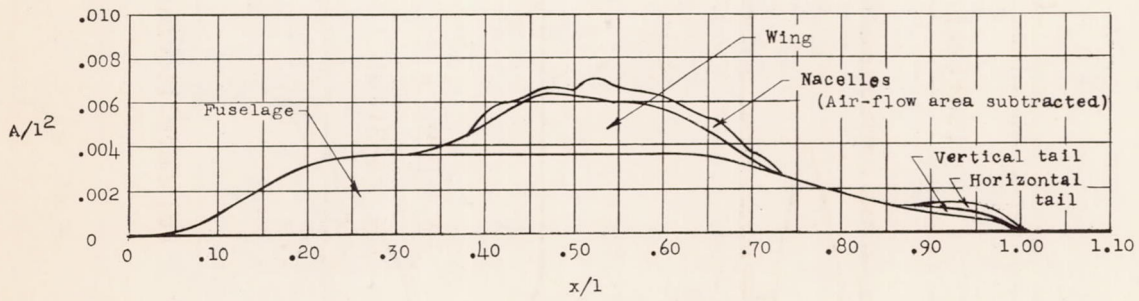

Area distribution

(c) Area-distribution and equivalent-body characteristics.

Figure 1.- Concluded.

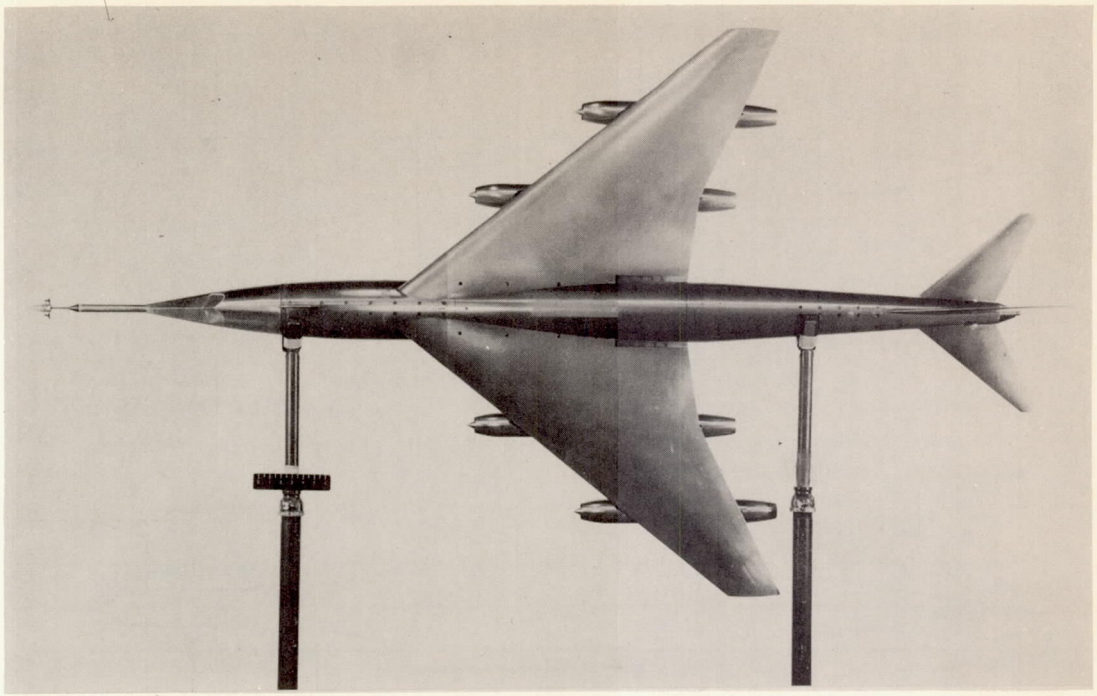

(a) Plan view. L-85271.1

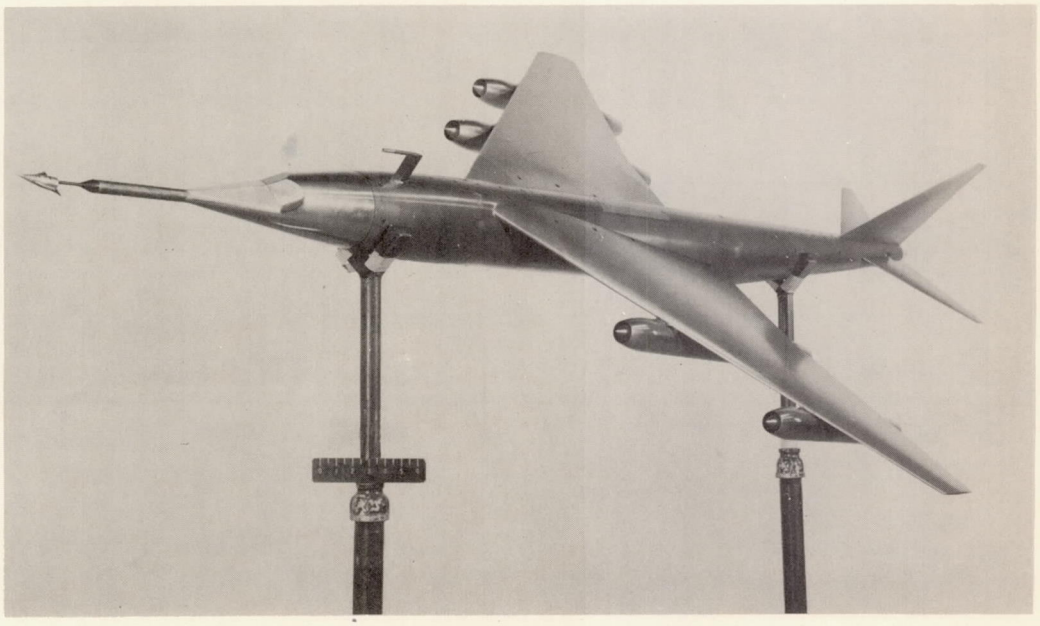

(b) Three-quarter front view. L-85269.1

Figure 2.- Photographs of the model.

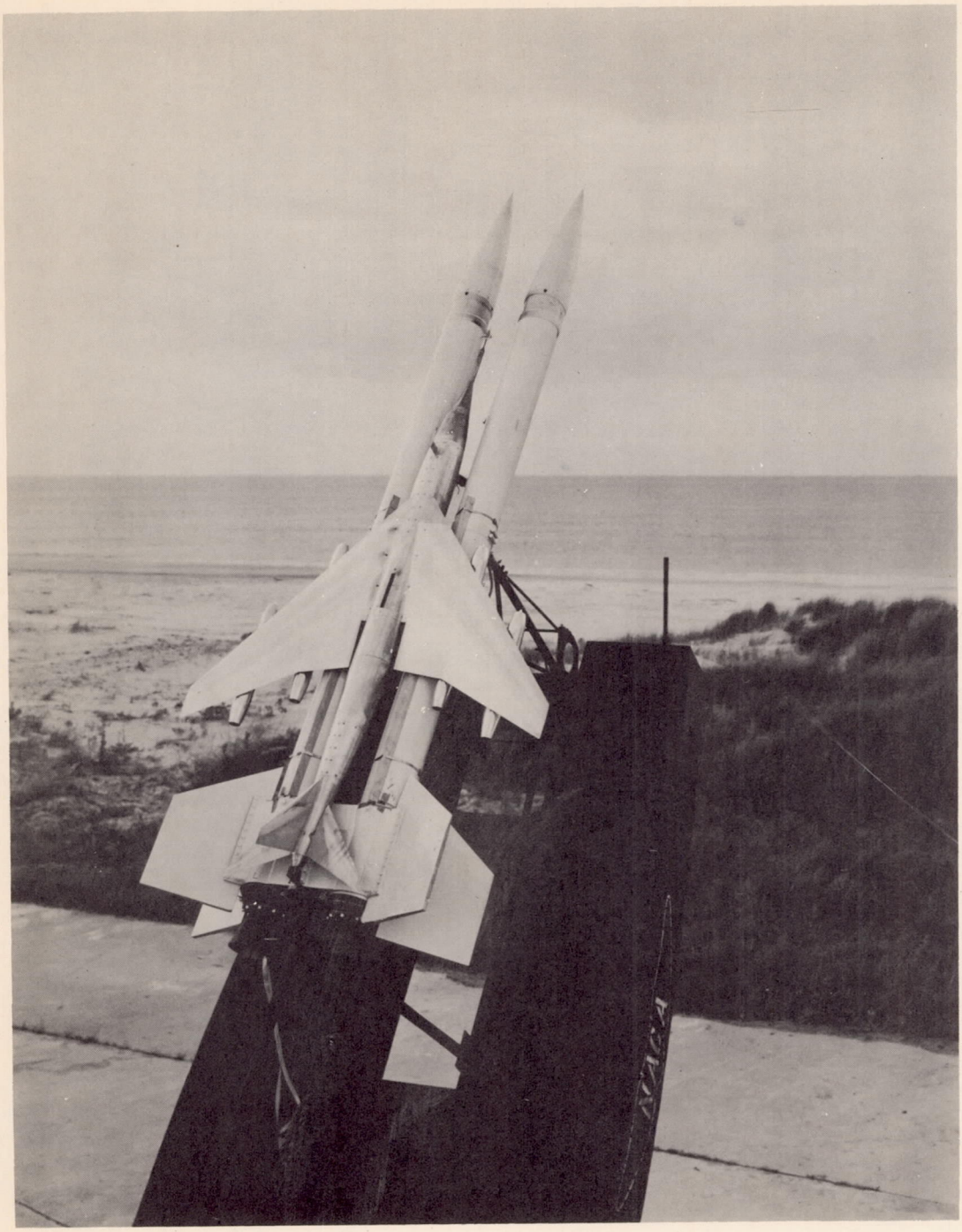

L-85751.1

(c) Model and booster on launcher.

Figure 2.- Concluded.

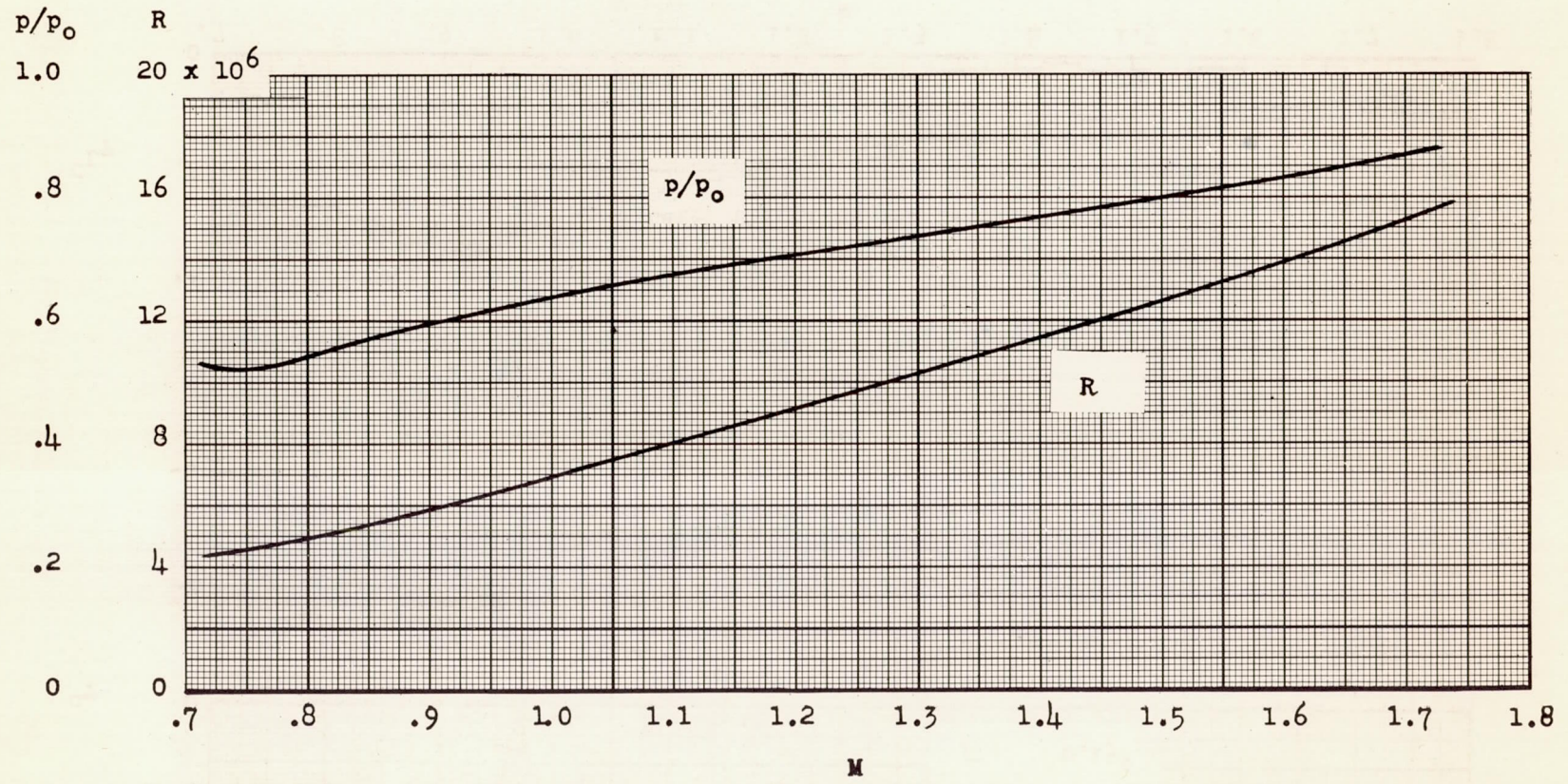

Figure 3.- Test conditions.

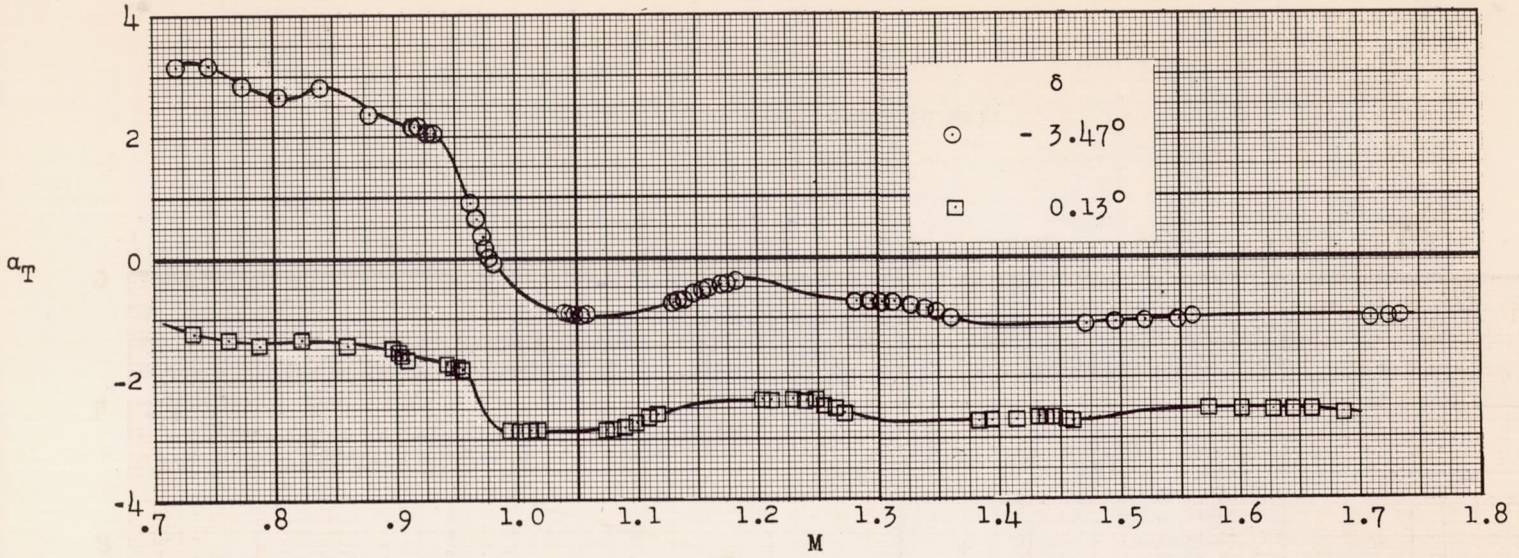

(a) Trim angle of attack.

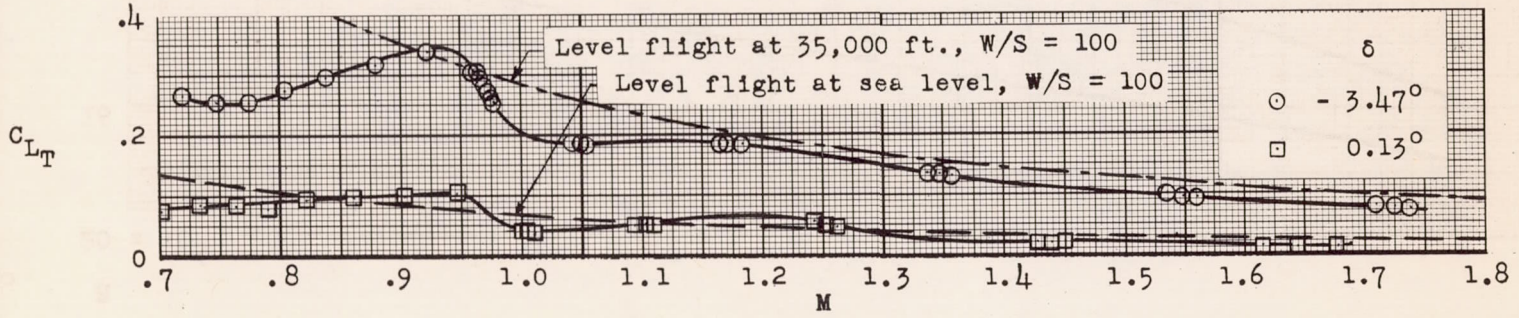

(b) Trim lift coefficient.

Figure 4.- Longitudinal trim characteristics.

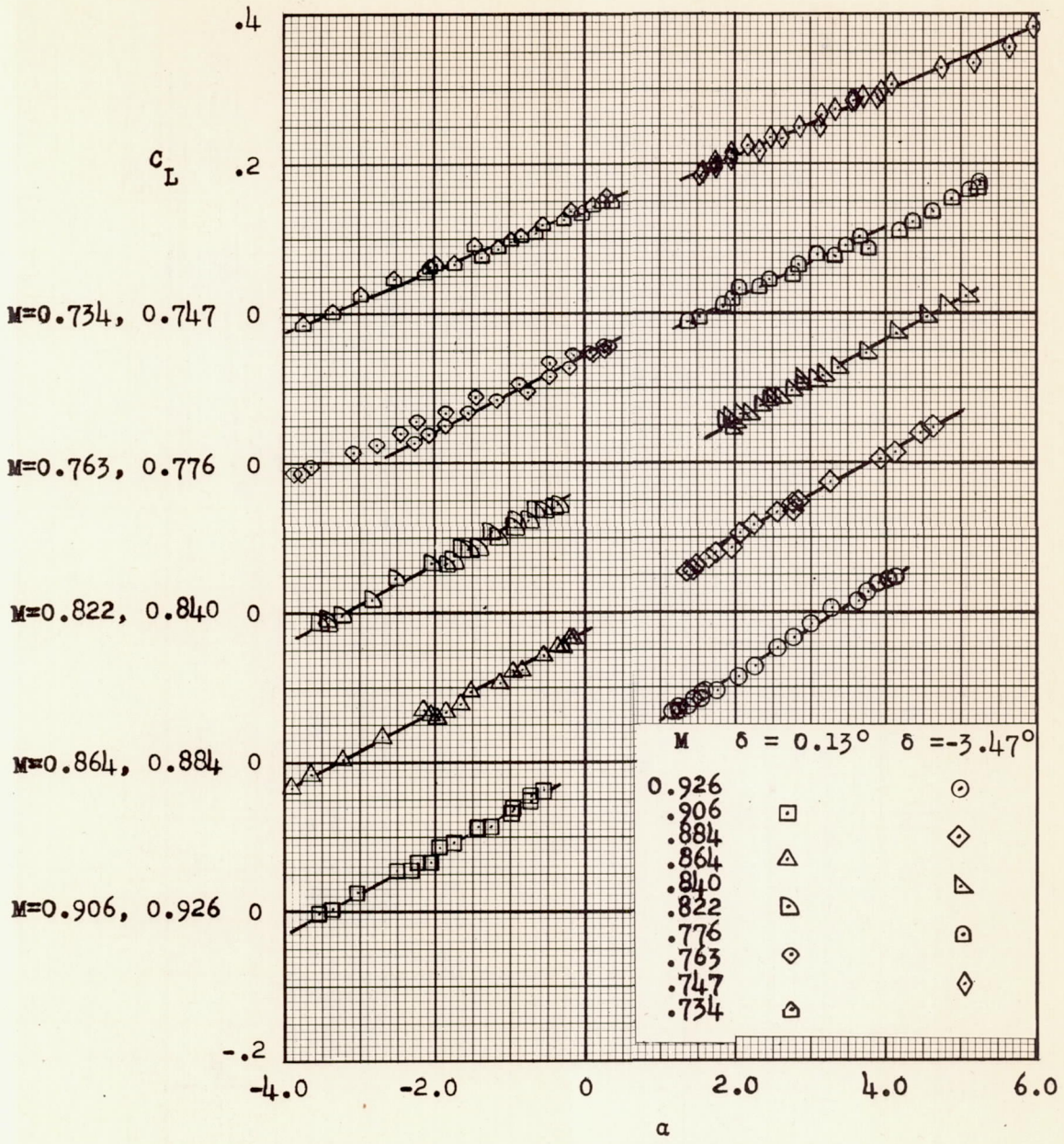

(a) Subsonic lift curves.

Figure 5.- Variation of lift coefficient with angle of attack.

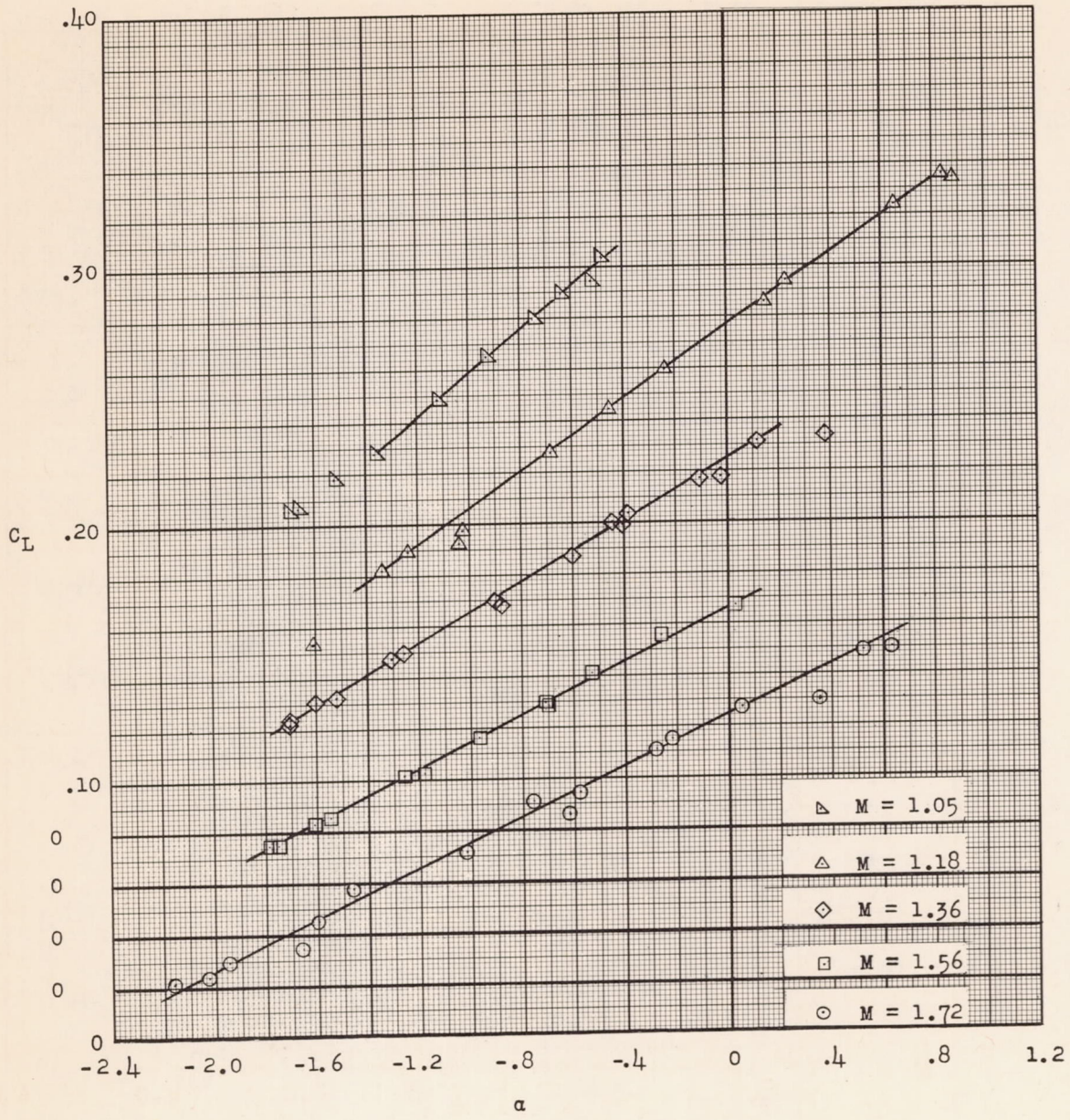

(b) Supersonic lift curves for $\delta = -3.47^{\circ}$.

Figure 5.- Continued.

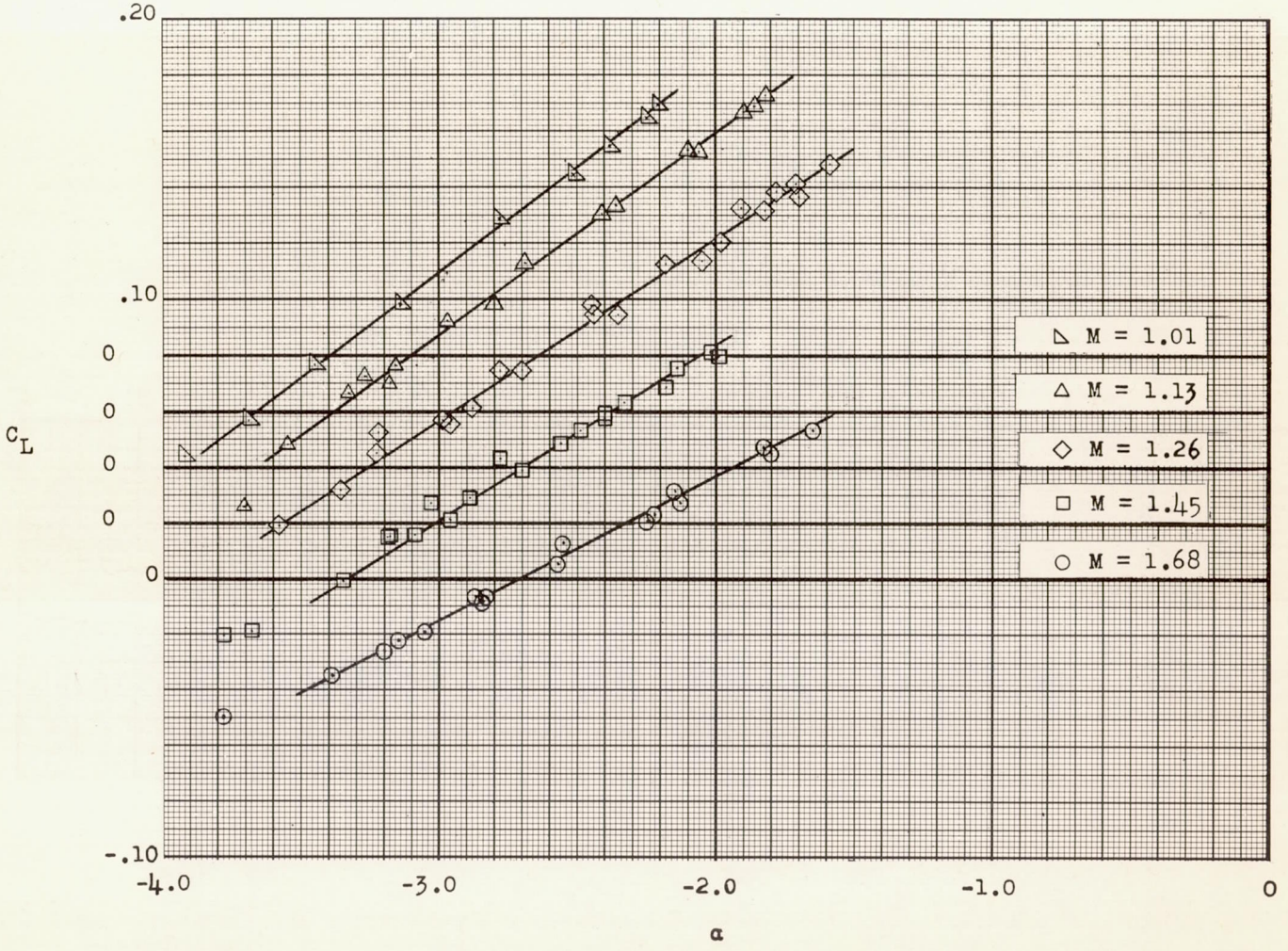

(c) Supersonic lift curves for $\delta = 0.13^{\circ}$.

Figure 5.- Concluded.

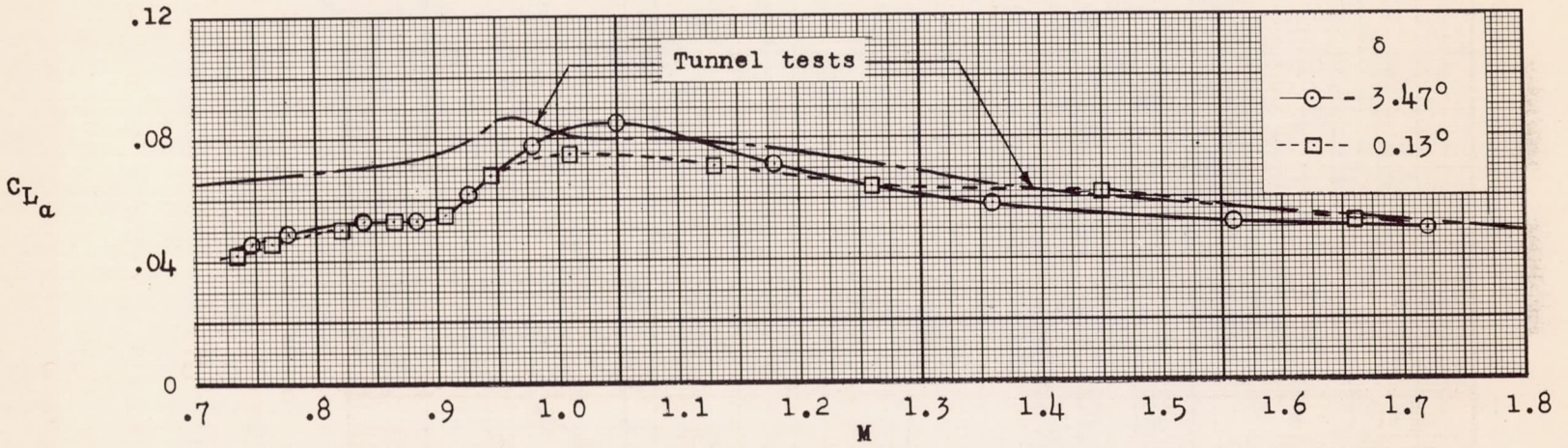

Figure 6.- Variation of lift-curve slope with Mach number.

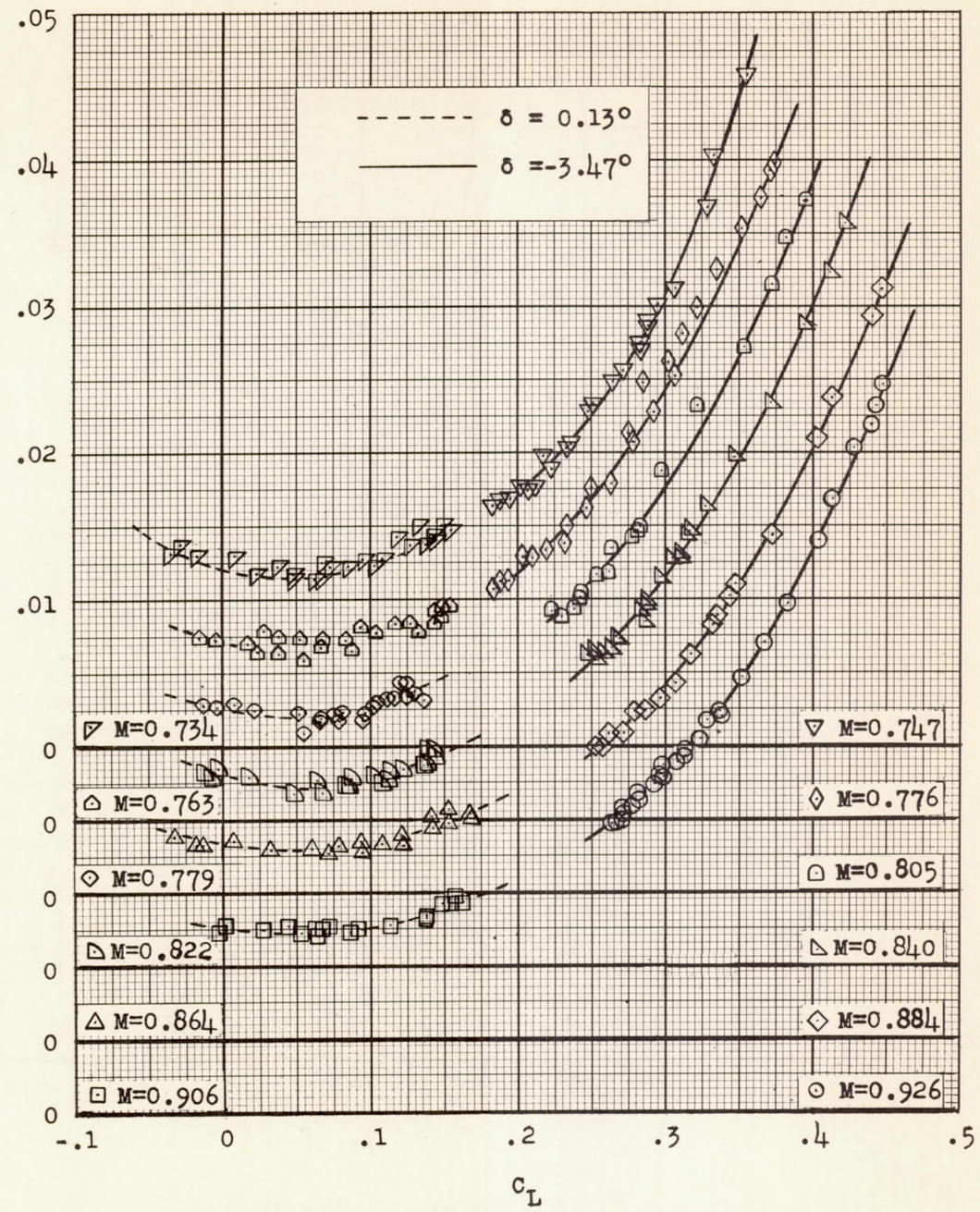

(a) Subsonic drag polars.

Figure 7.- Variation of drag with lift.

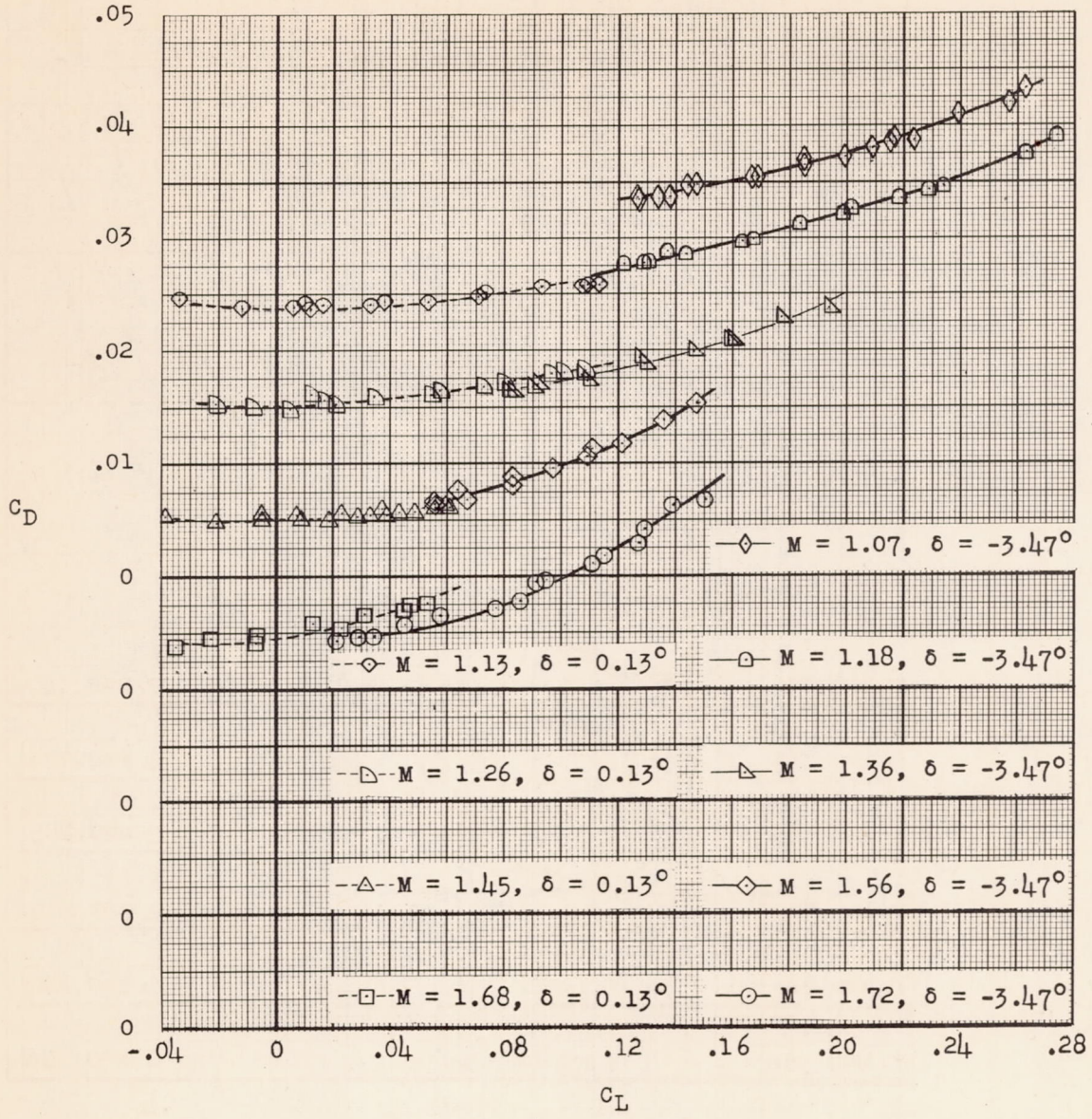

(b) Supersonic drag polars.

Figure 7.- Concluded.

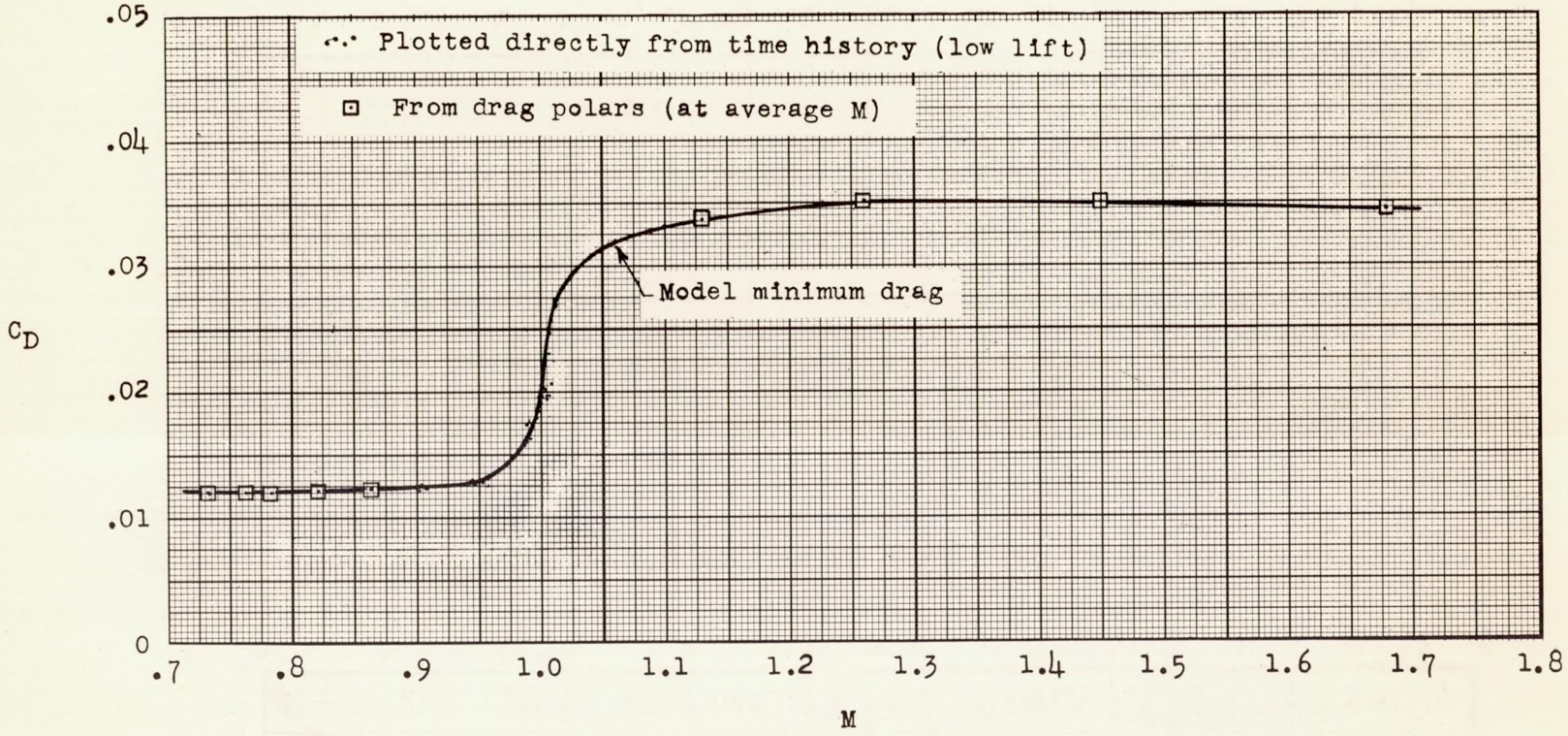

Figure 8.- Variation of drag with Mach number.

CONFIDENTIAL

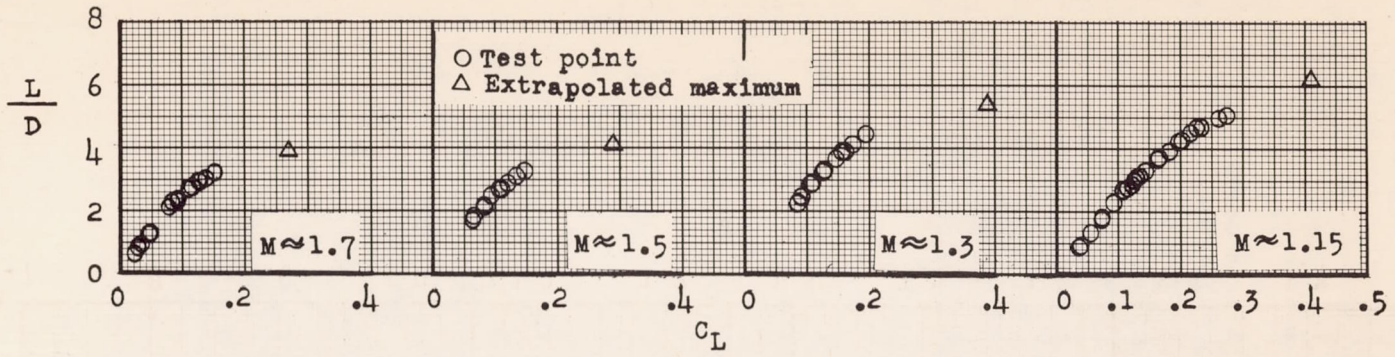

(a) Supersonic Mach numbers.

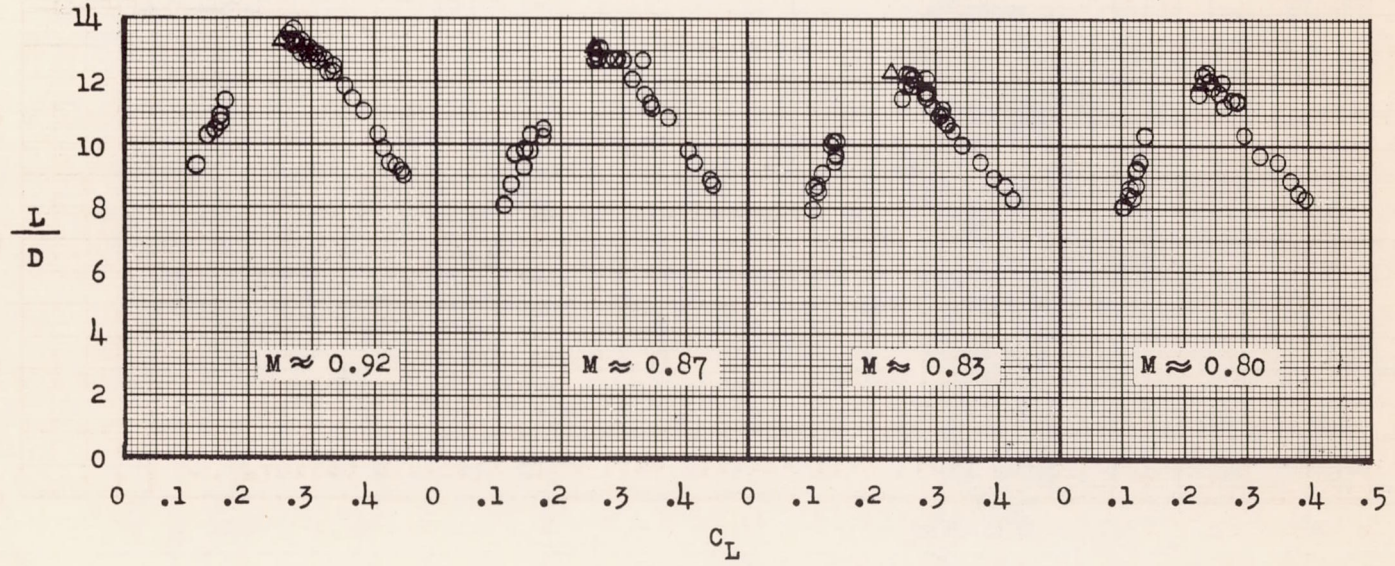

(b) Subsonic Mach numbers.

Figure 9.- Variation of L/D with lift coefficient.

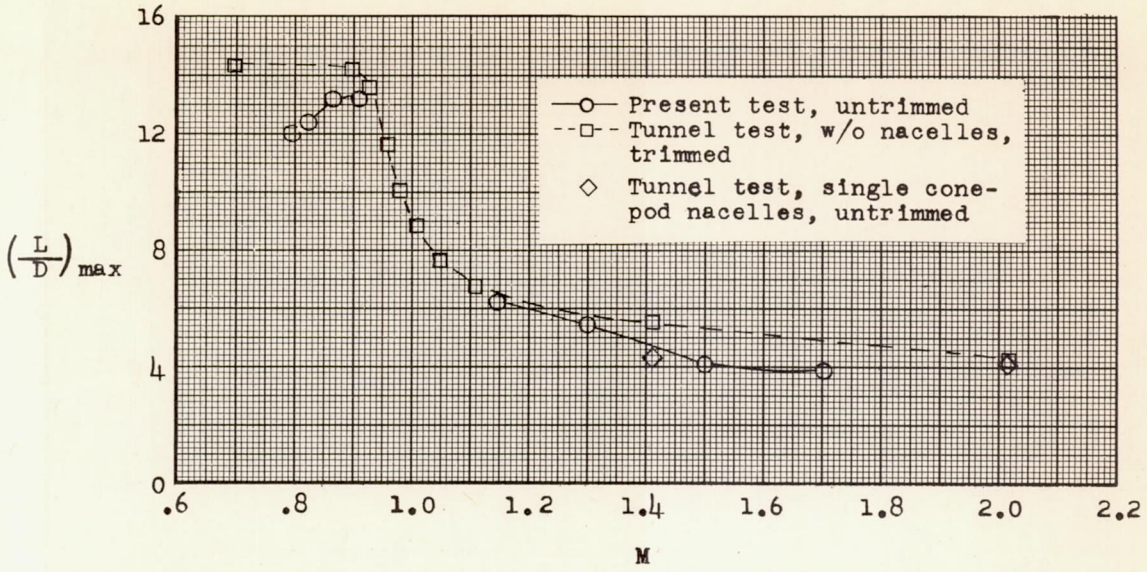

(a) Maximum lift-drag ratios.

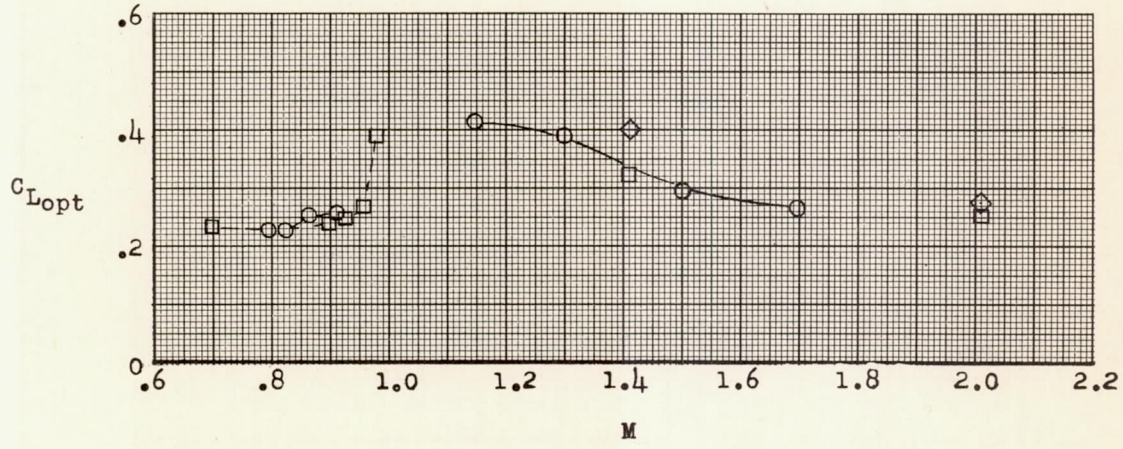

(b) Optimum lift coefficients.

Figure 10.- Variation of maximum lift-drag ratio and optimum lift coefficient with Mach number.

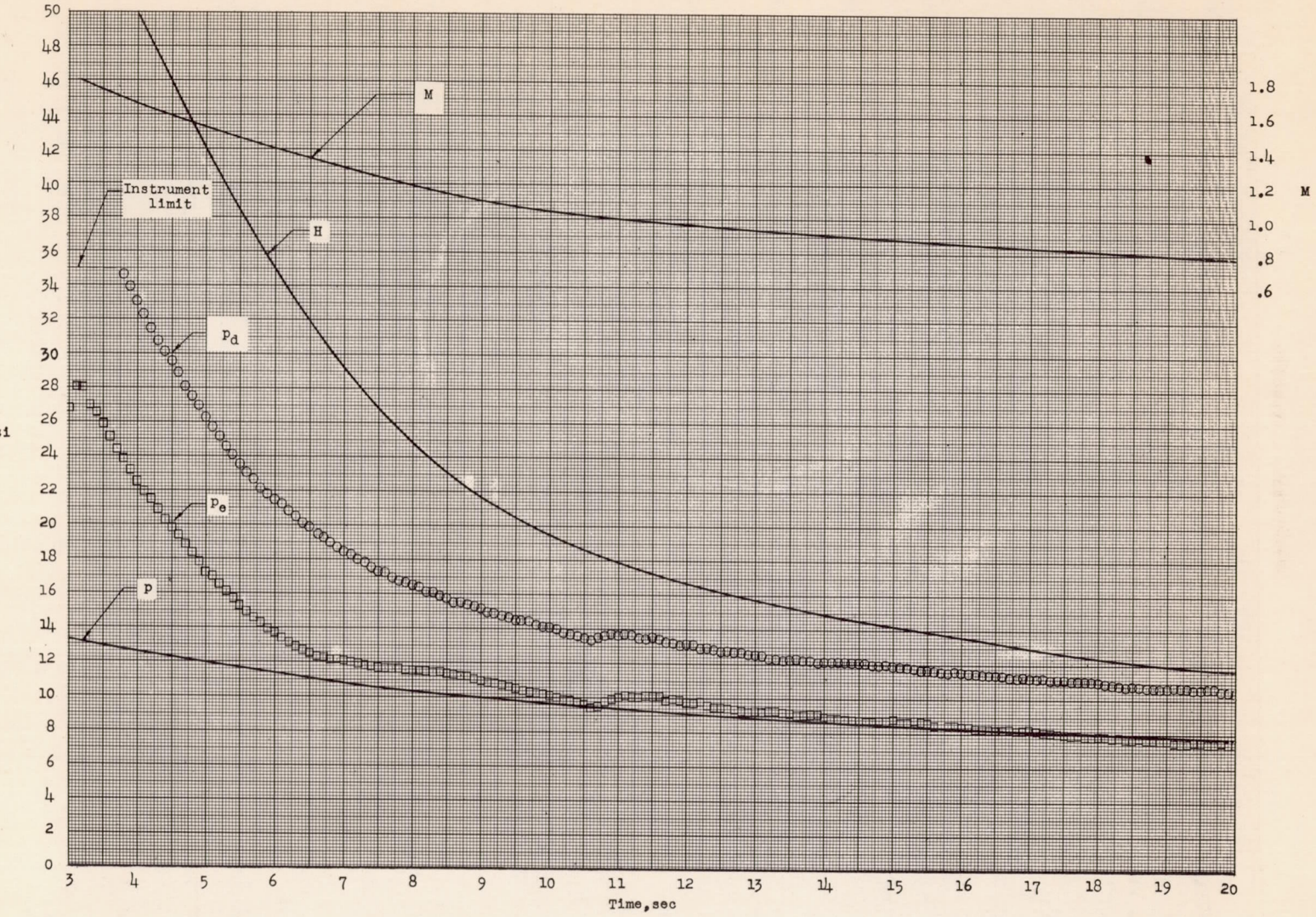

Figure 11.- Basic pressure data for determining nacelle characteristics.

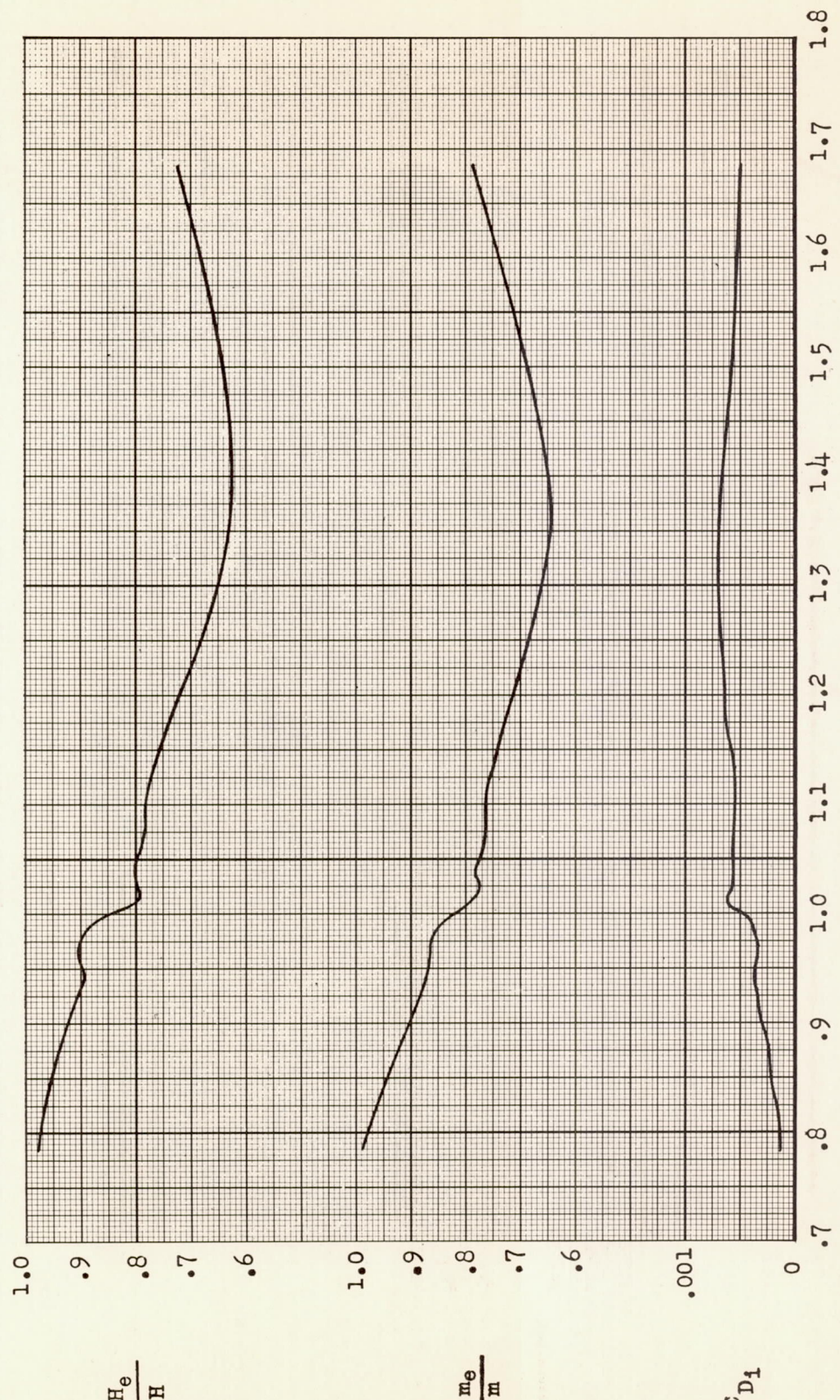

Figure 12.- Total-pressure recovery, mass-flow ratio, and internal-drag characteristics of the nacelles.

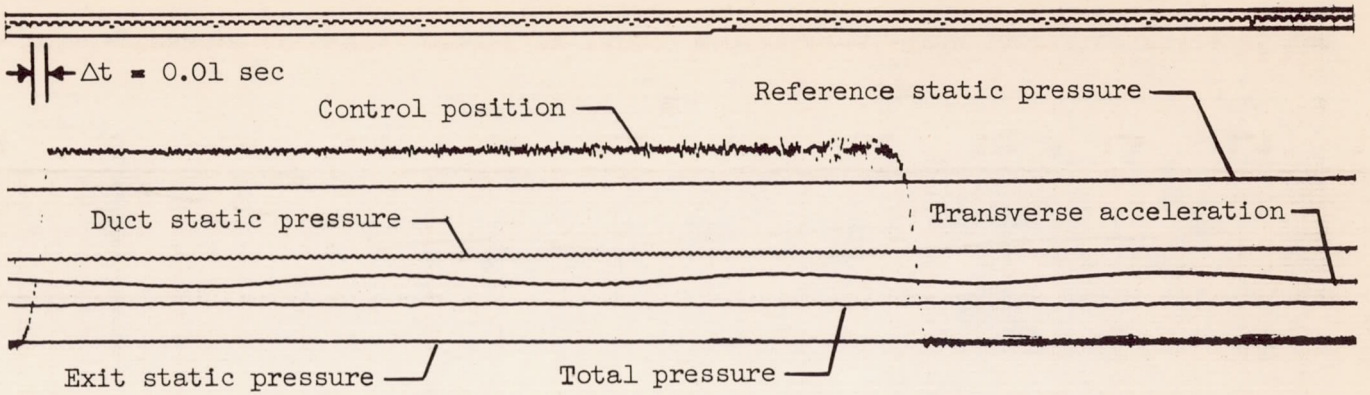

(a) Flight time from 11.3 seconds to 12.6 seconds.

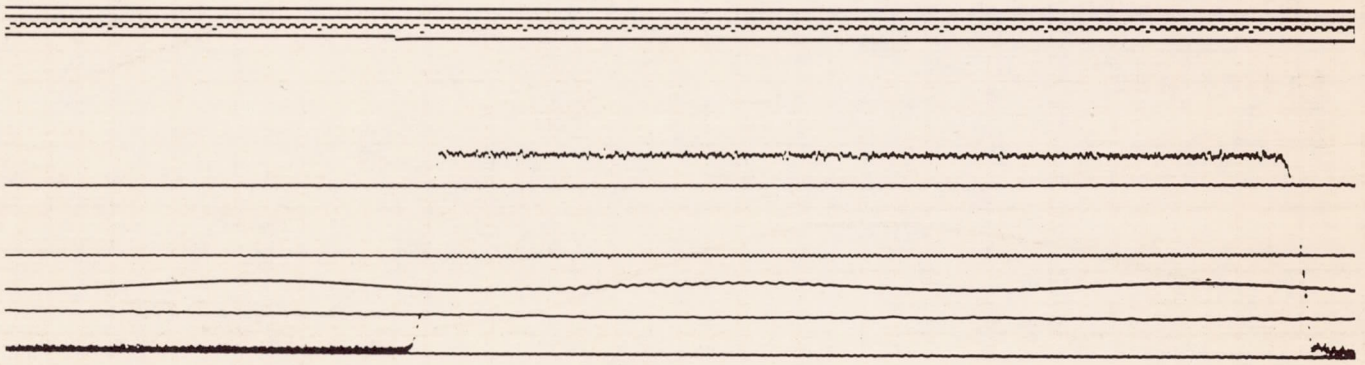

(b) Flight time from 12.6 seconds to 13.9 seconds.

Figure 13.- Sample telemeter record.

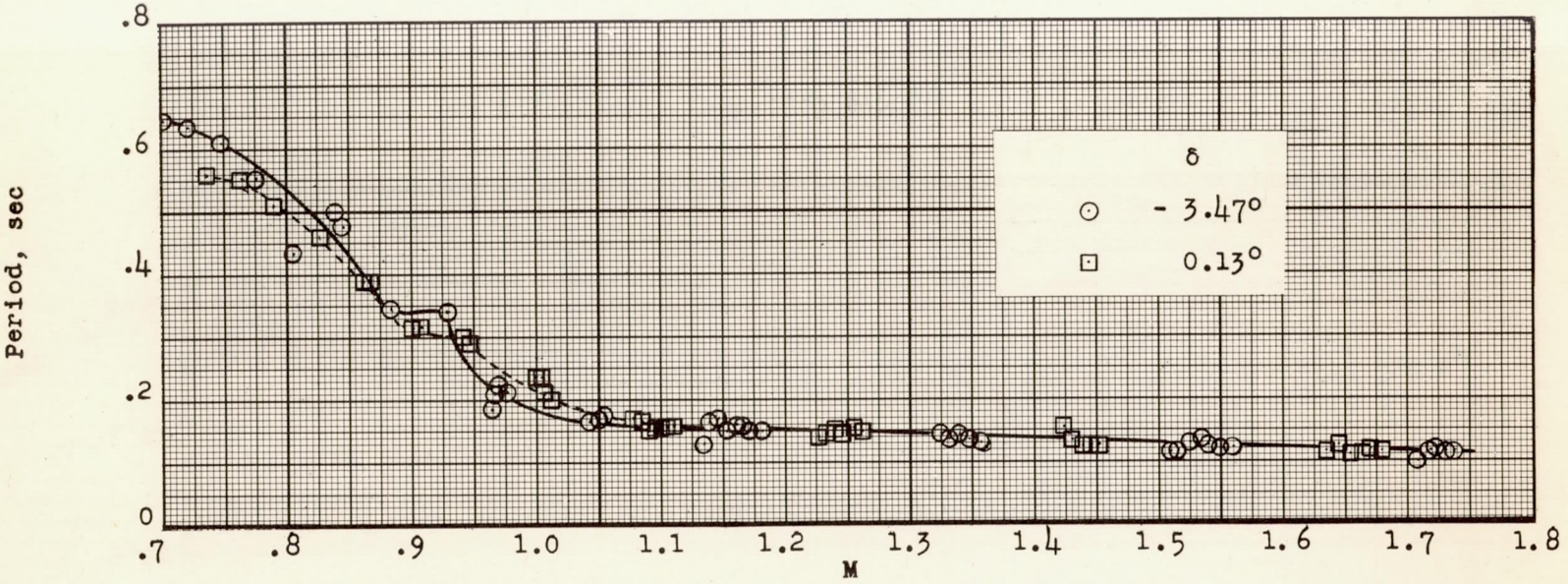

Figure 14.- Period of the longitudinal oscillation.

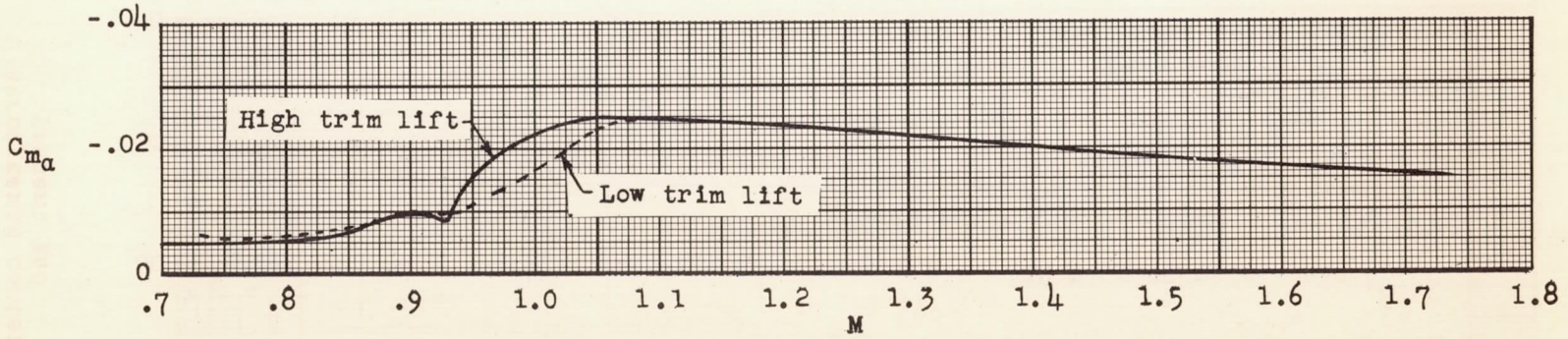

Figure 15.- Static longitudinal stability.

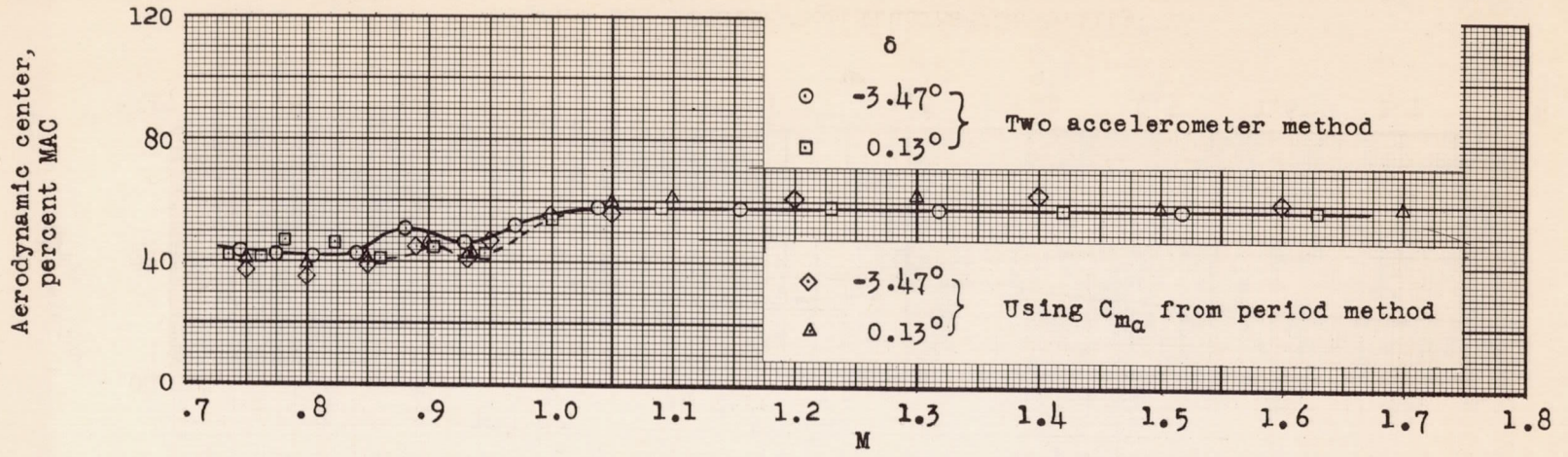

Figure 16.- Aerodynamic center location.

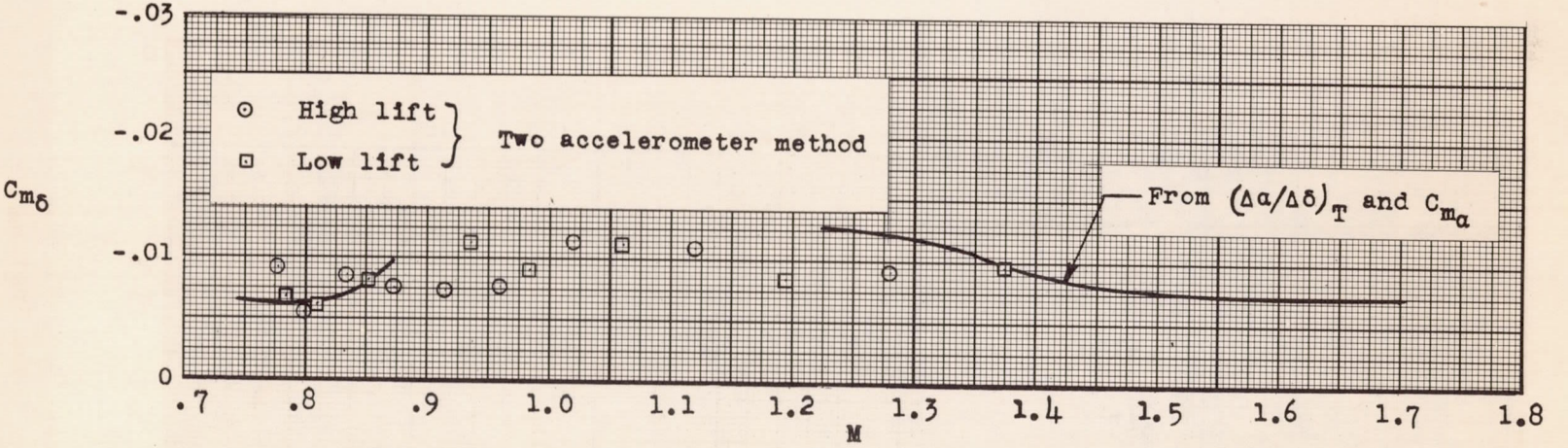

Figure 17.- Pitching moment effectiveness of the horizontal tail.

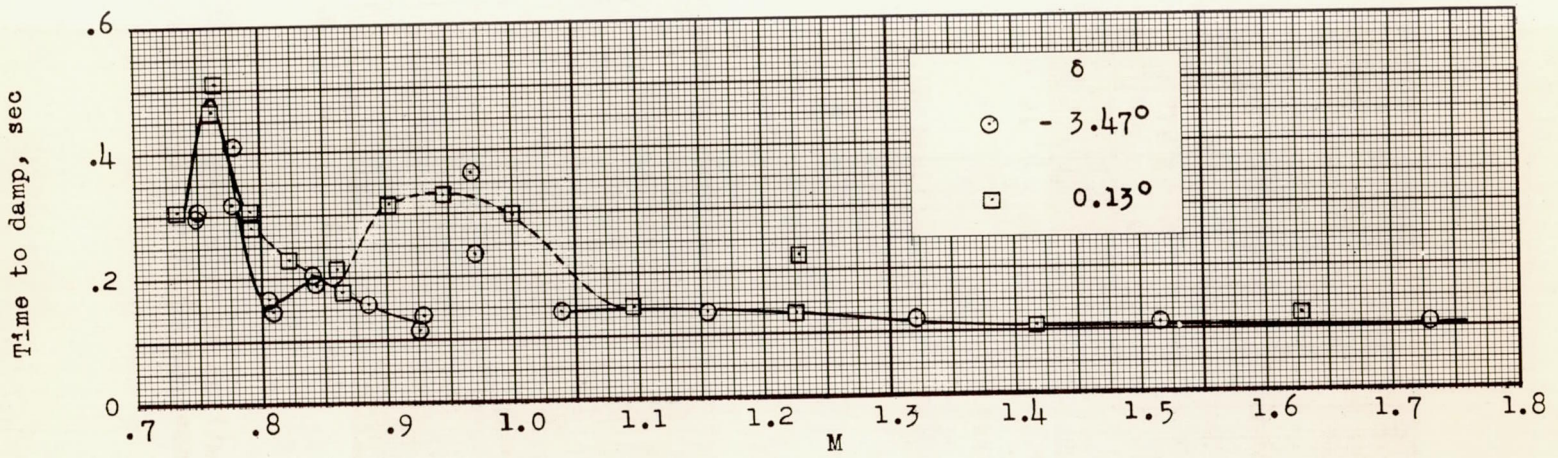

Figure 18.- Time to damp to one-half amplitude.

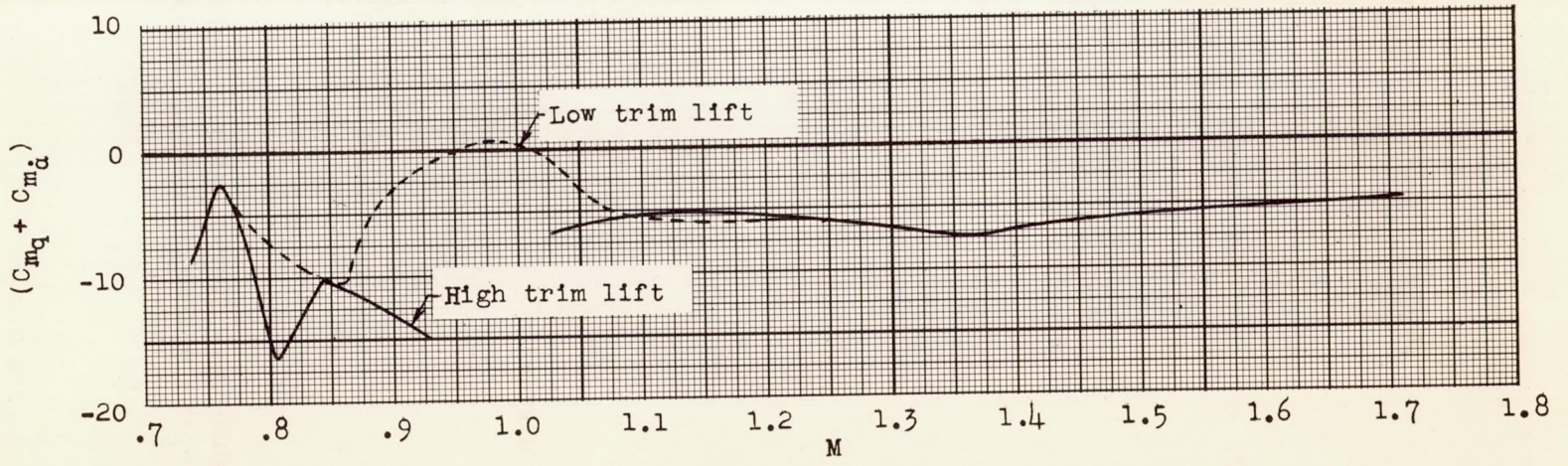

Figure 19.- Longitudinal dynamic stability.

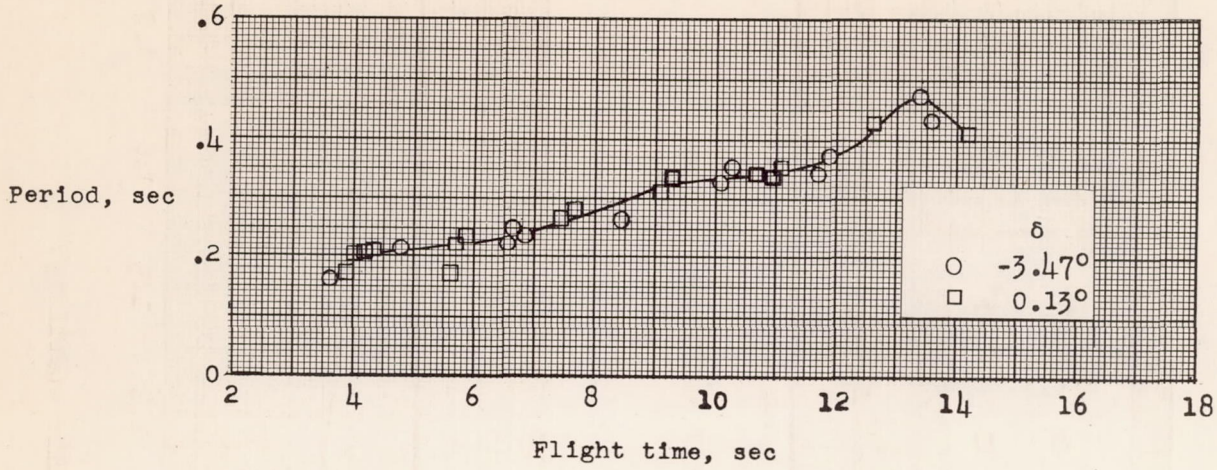

Figure 20.- Periods of the side-force oscillations.

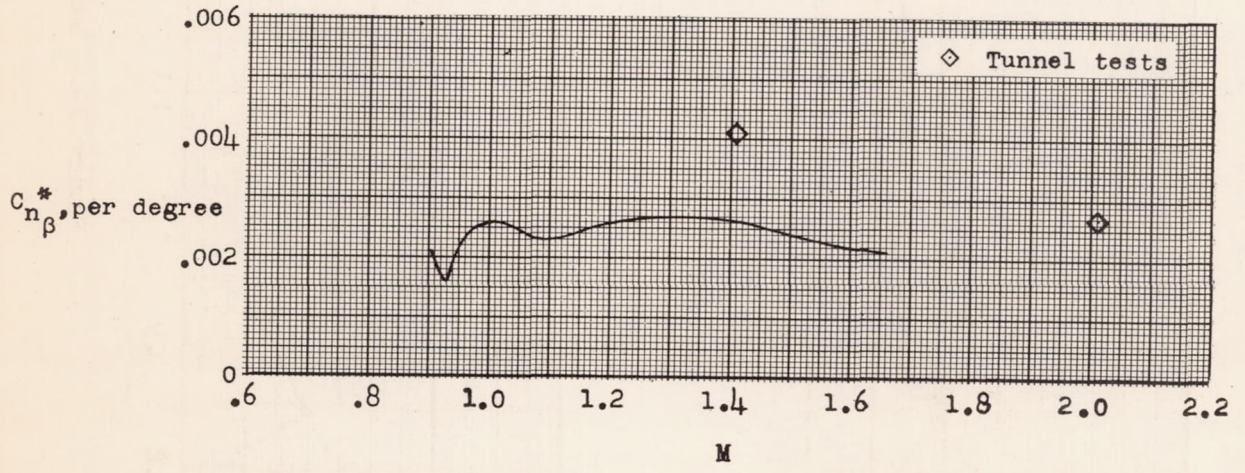

Figure 21.- Static lateral stability derivatives at trim lift from a one degree of freedom analysis. I_Z assumed equal to I_Y.

NACA - Langley Field, Va.